
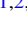




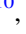









A Cosmological Fireball with 16% Gamma-Ray Radiative Efficiency

Liang Li^{1,2,3} , Yu Wang^{1,2,3} , Felix Ryde⁴ , Asaf Pe'er⁵ , Bing Zhang⁶ , Sylvain Guiriec^{7,8} , Alberto J. Castro-Tirado^{9,10} ,
D. Alexander Kann⁹ , Magnus Axelsson^{11,15} , Kim Page¹² , Péter Veres^{13,14} , and P. N. Bhat¹³ 

¹ICRANet, Piazza della Repubblica 10, I-65122 Pescara, Italy; liang.li@icranet.org

²INAF—Osservatorio Astronomico d'Abruzzo, Via M. Maggini snc, I-64100 Teramo, Italy; yu.wang@uniroma1.it

³Dip. di Fisica and ICRA, Sapienza Università di Roma, Piazzale Aldo Moro 5, I-00185 Rome, Italy

⁴Department of Physics, KTH Royal Institute of Technology, and the Oskar Klein Centre for Cosmoparticle Physics, SE-10691 Stockholm, Sweden

⁵Department of Physics, Bar-Ilan University, Ramat-Gan 52900, Israel

⁶Department of Physics and Astronomy, University of Nevada, Las Vegas, NV 89154, USA; zhang@physics.unlv.edu

⁷Department of Physics, The George Washington University, 725 21st Street NW, Washington, DC 20052, USA

⁸NASA Goddard Space Flight Center, Greenbelt, MD 20771, USA

⁹Instituto de Astrofísica de Andalucía (IAA-CSIC), PO Box 03004, E-18008 Granada, Spain

¹⁰Departamento de Ingeniería de Sistemas y Automática, Escuela de Ingenierías, Universidad de Málaga, Málaga, Spain

¹¹Department of Astronomy, Stockholm University, SE-10691 Stockholm, Sweden

¹²School of Physics and Astronomy, University of Leicester, University Road, Leicester, LE1 7RH, UK

¹³Center for Space Plasma and Aeronomic Research, University of Alabama in Huntsville, Huntsville, AL, USA

¹⁴Space Science Department, University of Alabama in Huntsville, Huntsville, AL, USA

Received 2022 November 17; revised 2023 January 30; accepted 2023 February 6; published 2023 February 23

Abstract

Gamma-ray bursts (GRBs) are the most powerful explosions in the universe. How efficiently the jet converts its energy to radiation is a long-standing problem, which is poorly constrained. The standard model invokes a relativistic fireball with a bright photosphere emission component. A definitive diagnosis of GRB radiation components and the measurement of GRB radiative efficiency require prompt emission and afterglow data, with high resolution and wide band coverage in time and energy. Here, we present a comprehensive temporal and spectral analysis of the TeV-emitting bright GRB 190114C. Its fluence is one of the highest for all the GRBs that have been detected so far, which allows us to perform a high-resolution study of the prompt emission spectral properties and their temporal evolutions, down to a timescale of about 0.1 s. We observe that each of the initial pulses has a thermal component contributing $\sim 20\%$ of the total energy and that the corresponding temperature and inferred Lorentz factor of the photosphere evolve following broken power-law shapes. From the observation of the nonthermal spectra and the light curve, the onset of the afterglow corresponding to the deceleration of the fireball is considered to start at ~ 6 s. By incorporating the thermal and nonthermal observations, as well as the photosphere and synchrotron radiative mechanisms, we can directly derive the fireball energy budget with little dependence on hypothetical parameters, measuring a $\sim 16\%$ radiative efficiency for this GRB. With the fireball energy budget derived, the afterglow microphysics parameters can also be constrained directly from the data.

Unified Astronomy Thesaurus concepts: [Gamma-ray bursts \(629\)](#)

1. Introduction

On 2019 January 14 at 20:57:02.63 universal time (hereafter, T_0), an ultrabright burst, GRB 190114C, first triggered the Gamma-ray Burst Monitor (GBM) on board the Fermi Gamma-ray Space Telescope (Hamburg et al. 2019) and the Burst Alert Telescope (BAT) of the Neil Gehrels Swift Observatory (hereafter, Swift; Gropp et al. 2019). Soon after, the Large Area Telescope (LAT) on board Fermi, Konus-Wind, INTEGRAL/SPI-ACS, AGILE/MCAL, and the Insight-HXMT/HE were also triggered. Long-lasting multiwavelength afterglow observations were carried out by the Major Atmospheric Gamma Imaging Cherenkov (MAGIC) telescopes (MAGIC Collaboration et al. 2019b) in the teraelectronvolt band, by Swift in the X-ray and optical bands, and by several ground-based optical and radio telescopes, such as GROND (Bolmer & Schady 2019), Gran Telescopio CANARAS

(Castro-Tirado et al. 2019), the Very Large Array (VLA; Alexander et al. 2019), and MeerKAT (Tremou et al. 2019).

In this paper, we present a comprehensive analysis of GRB 190114C and derive fireball parameters, using rich observation data. The paper is organized as follows. In Section 2, we outline the main observing properties of the burst and the purpose of the paper. The methodology is presented in Section 3. The models that apply to GRB 190114C are presented in Section 4. We present our results in Section 5. Our conclusions are summarized in Section 6. Throughout the paper, we adopt the standard Λ CDM cosmology, with the parameters $H_0 = 67.4 \text{ km s}^{-1} \text{ Mpc}^{-1}$, $\Omega_M = 0.315$, and $\Omega_\Lambda = 0.685$ (Planck Collaboration et al. 2020).

2. Overview

The T_{90} duration¹⁶ reported by the Fermi term is ~ 116 s, so GRB 190114C therefore belongs to the class of long-duration bursts. The 1024 ms peak flux and the fluence during the T_{90} duration at 10–1000 keV as measured by Fermi-GBM are $246.9 \pm 0.9 \text{ photon cm}^{-2} \text{ s}^{-1}$ and $(4.436 \pm 0.005) \times 10^{-4} \text{ erg cm}^{-2}$, respectively. A measured redshift of $z = 0.424$

¹⁵ Deceased.

¹⁶ The time taken to accumulate 90% of the burst fluence starts at the 5% fluence level and ends at the 95% fluence level.

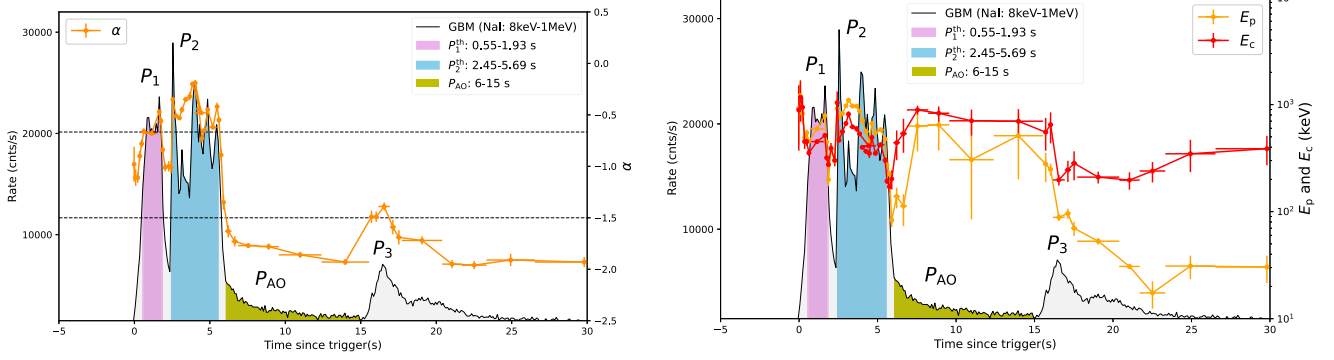


Figure 1. Count light curves of Fermi-GBM during the time span of 0–30 s. The differently shaded regions marked with different colors denote the two independent thermally subdominated episodes: P_1^{th} (pink) and P_2^{th} (blue), the afterglow emission episode P_{AO} (yellow), and the gamma-ray flare emission P_3 (gray). Left: the two horizontal dashed lines represent the limiting values of $\alpha = -2/3$ and $\alpha = -3/2$ for electrons in the synchrotron slow- and fast-cooling regimes, respectively. The data points that are connected by the solid orange lines represent the temporal evolution of the low-energy photon index α of the CPL-only fits. Right: the data points that are connected by the solid orange lines represent the temporal evolution of E_p for the Band-only fits, while those in red indicate the temporal evolution of the E_c for the CPL-only fits.

was announced by Castro-Tirado et al. (2019); therefore, the isotropic equivalent gamma-ray energy with a k -correction to the rest-frame ($1\text{--}10^4$ keV) is estimated to be $E_{\gamma,\text{iso}} = (2.8 \pm 0.3) \times 10^{53}$ erg. Fermi-LAT observed the first GeV photon at $T_0 + 2.1$ s and the highest-energy photon is a 22.9 GeV event that was observed at $\sim T_0 + 15$ s (Wang et al. 2019b). The afterglow emission measured by the X-ray Telescope (XRT) on Swift begins at $\sim T_0 + 68$ s.

The prompt emission light curve consists of three distinct emission pulses (Figure 1; Wang et al. 2019b; Ajello et al. 2020). The first pulse (i.e., P_1) starts at $\sim T_0$ and lasts for ~ 2.35 s; the second pulse (i.e., P_2) exhibits multiple peaks and lasts from $\sim T_0 + 2.35$ s to $\sim T_0 + 6$ s; and the significantly fainter third pulse (i.e., P_3) extends from $\sim T_0 + 15$ s to $\sim T_0 + 25$ s. A majority of the α indices in P_1 and P_2 are beyond the line-of-death of synchrotron emission ($-2/3$; Preece et al. 1998), suggesting the origin of the photosphere emission. Such a feature is observed in GRB 190114C and it is fully consistent with what the fireball photosphere model predicts. In the standard gamma-ray burst (GRB) fireball model–external shock model (Rees & Meszaros 1994; Mészáros & Rees 2000), after a relativistic jet is launched from a central engine, the energy can either be dissipated by: (1) early short-lived prompt emissions (generated by photosphere emissions where the jet becomes transparent or by an internal shock via synchrotron emission) that occur at a close distance from the progenitor and are mostly observed in gamma rays; or (2) later long-lasting multiwavelength afterglow emissions (generated by an external shock at a large distance from where the GRB jets interact with the ambient medium) that are observed at X-ray, optical, and radio wavelengths. Therefore, a bright thermal component originating from the fireball photosphere and a nonthermal component presumably originating from internal shocks with radii greater than the photosphere radius would be expected to be observed in the prompt emission spectra. The emission in P_3 can be interpreted as a flare of synchrotron radiation. However, the flux, energy band, and power-law decay index (Figure 2) during the epoch from $\sim T_0 + 6$ s to $\sim T_0 + 15$ s (i.e., P_{AO}) between P_2 and P_3 are consistent with the external shock emission at $t_{\text{onset}} \approx 6$ s, defined by the deceleration of the fireball, where P_{AO} represents the initialization of the afterglow emission phase generated by the deceleration of the fireball and t_{onset} represents the onset time of the deceleration of the fireball.

The proposal that P_{AO} is related to the afterglow emission is supported by several independent studies in the literature (e.g., MAGIC Collaboration et al. 2019b; Ravasio et al. 2019; Ajello et al. 2020; Ursi et al. 2020). Onset signatures of afterglow emission that are observed in the MeV energy range during the prompt emission phase are rare, since they are typically observed as deceleration bumps in the early afterglow light curve (e.g., Liang et al. 2010, 2013). The afterglow phase of this GRB has the most comprehensive observations in terms of spectral coverage (see Figure 3), from radio to TeV gamma rays (MAGIC Collaboration et al. 2019b; Ravasio et al. 2019). This provides a unique opportunity to study the GRB afterglow properties within the framework of the synchrotron and synchrotron self-Compton model (MAGIC Collaboration et al. 2019a). Moreover, by combining the observed properties of the thermal emission in the first two episodes and the nonthermal emission in the third episode, GRB 190114C may be the first case that provides us with a unique opportunity of dissecting the energy budget of a GRB fireball.

Another interesting subject relating to the GRB prompt emission mechanism, which describes how efficiently the jet converts its energy to radiation, is the radiative efficiency of a burst. The GRB radiative efficiency may be defined as (Lloyd-Ronning & Zhang 2004)

$$\eta_{\gamma} \equiv \frac{E_{\gamma}}{E_{\text{tot}}} = \frac{E_{\gamma}}{E_{\gamma} + E_k} = \frac{L_{\gamma}}{L_{w,0}}, \quad (1)$$

where E_{γ} , E_k , and E_{tot} are the isotropic equivalent gamma-ray energy, the afterglow kinetic energy, and the total energy, respectively, and L_{γ} and $L_{w,0}$ are the isotropic equivalent average gamma-ray luminosity and the total wind luminosity at the central engine, respectively. In order to evaluate the radiative efficiency of a GRB, according to Equation (1), one needs to know the isotropic equivalent gamma-ray energy E_{γ} and the blastwave kinetic energy E_k . The E_{γ} term can be measured from the spectral parameters. The E_k term, on the other hand, is usually estimated from afterglow data through modeling, but the estimated values typically have large uncertainties (Zhang et al. 2007). By combining the prompt emission and early afterglow data, Zhang et al. (2021) proposed a new method for directly dissecting the GRB fireball energy budget into three components and measuring

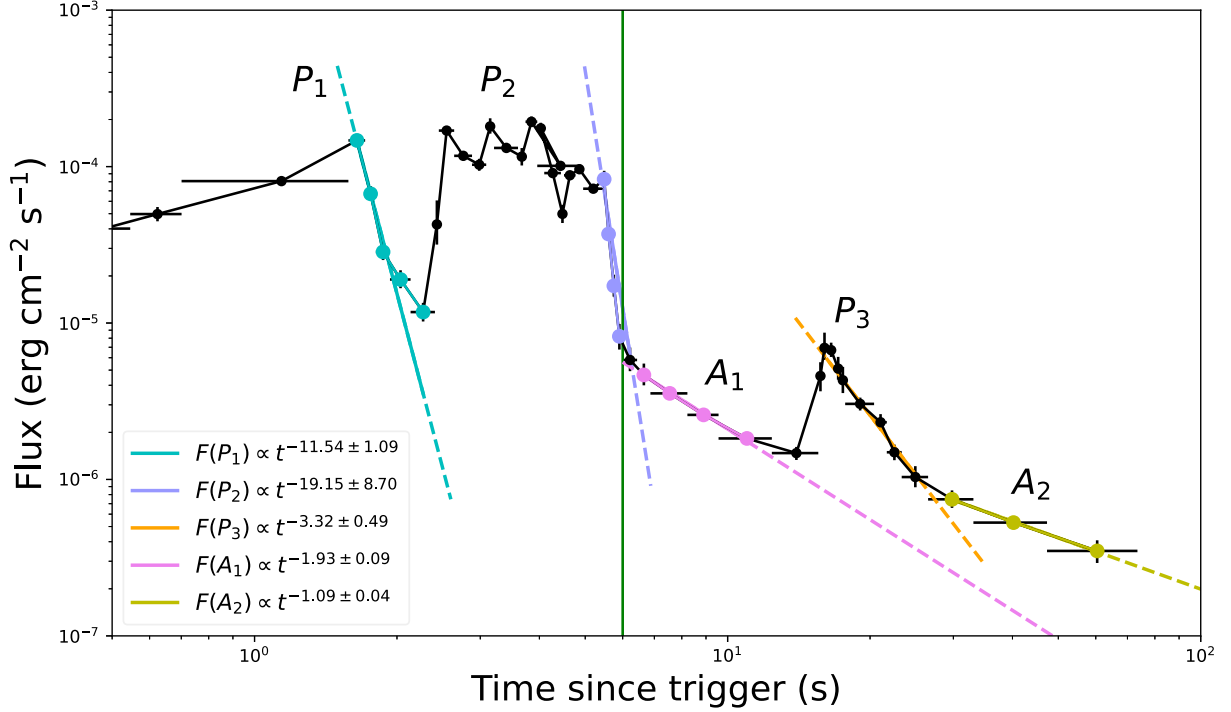


Figure 2. The GBM light curve (dotted black line) with best fits to the decay phases of P_1 (cyan), P_2 (magenta), P_3 (orange), and the afterglow emission A_1 (violet) and A_2 (yellow), using a single PL model. Note that A_1 and A_2 correspond to the afterglow emission generated by P_1 and P_2 , respectively. The onset of the afterglow emission $t_{\text{Afterglow}}$ (vertical green line) is used to estimate Γ in Equation (12). The decay index of the afterglow emission from P_1 is $\hat{\alpha}(A_1) = -1.93 \pm 0.09$, which is significantly steeper than the typical value for afterglow emission measured from other GRBs. This is because some of the energy flux in this segment is clearly contributed from P_2 , whereas the decay index of the afterglow emission from P_2 is $\hat{\alpha}(A_2) = -1.09 \pm 0.04$, which is in good agreement with the typical values found for afterglow emission.

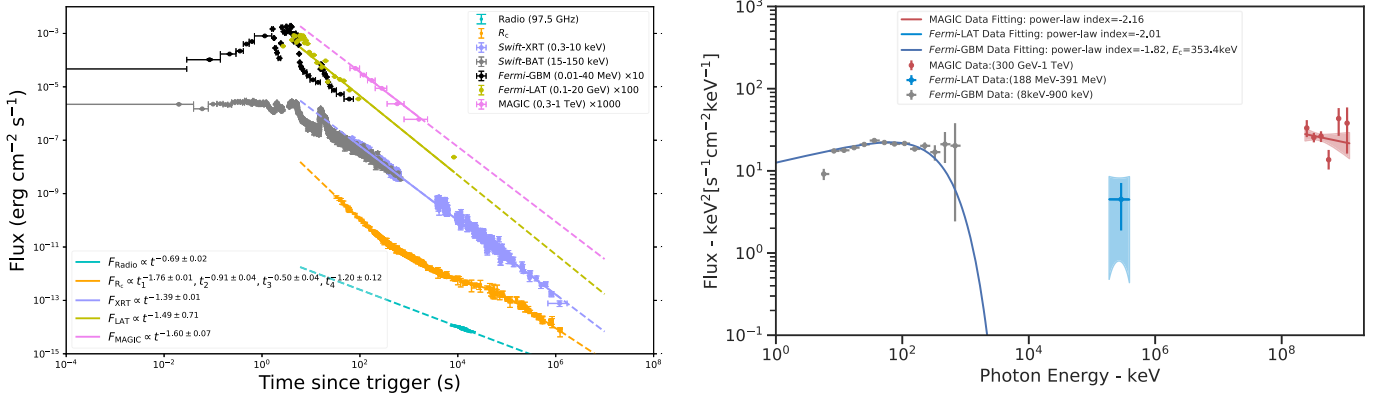


Figure 3. Left: multiwavelength light curve. The data points indicated in violet, yellow, black, gray, magenta, orange, and cyan represent the MAGIC, Fermi-LAT, Fermi-GBM, Swift-BAT, Swift-XRT, optical (R_c -band), and radio (at 97.5 GHz) observations, respectively. The solid lines show the best power-law fits to the data. Note that: (1) the LAT data are separated into two parts at ~ 6 s and we only fit the second (afterglow) part (> 6 s) here; (2) the optical R_c band has been corrected for Galactic and host extinction, and the contribution from the host galaxy has also been subtracted. This light curve has been created by shifting data from different bands to the R band. Right: multiwavelength spectrum, covering the energy in the MeV (gray), GeV (blue), and TeV (jacinth) emission, as simultaneously observed from T_0+68 s to T_0+110 s by Fermi-GBM, Fermi-LAT, and MAGIC, respectively.

their values. As a result, the GRB radiation efficiency can also be directly calculated with little uncertainty. The method requires a GRB with a dominant thermal spectral component, a deceleration bump feature in the early afterglow light curve, and a measured redshift. The measured parameters include the initial dimensionless specific enthalpy (η), the bulk Lorentz factors at the photosphere radius (Γ_{ph}) and before fireball deceleration (Γ_0), the amount of mass loading (M), and the GRB radiative efficiency (η_γ). These measured parameters only

weakly depend on the density n of the interstellar medium when the composition \mathcal{Y} parameter (typically unity) is specified, where \mathcal{Y} is the lepton-to-baryon number ratio, which equals unity for a pure hydrogen fireball, but could be greater (for a pair-loaded fireball) or slightly smaller (for a neutron-rich fireball without pair loading) than unity.

Once these fireball parameters can be precisely measured, one can also estimate the blastwave kinetic energy as $E_K = \Gamma_0 M c^2$, as well as the GRB radiative efficiency η_γ . In

Table 1

Comparison of Δ DIC Values between the Best Model (CPL+BB) and Various Other Models (PL, BB, CPL, Band, SBKPL, PL+BB, and PL+Bandcut) in GRB 190114C, Based on the Time-integrated Spectral Analysis

$t_1 \sim t_2$	Δ DIC(1)	Δ DIC(2)	Δ DIC(3)	Δ DIC(4)	Δ DIC(5)	Δ DIC(6)	Δ DIC(7)
(s)	(CPL+BB-PL)	(CPL+BB-BB)	(CPL +BB-CPL)	(CPL +BB-Band)	(CPL+BB- SBKPL)	(CPL+BB)- (PL+BB)	(CPLBB)-(PL +Bandcut)
0~116	-3523	-19565	-266	-262	-34	-457	-68

this paper, using the photosphere data observed in P_1 and P_2 , and the early afterglow data observed in P_{AO} , as supported by several independent studies in the literature, as well as a measured redshift, we apply the method proposed in Zhang et al. (2021) for directly dissecting the GRB fireball energy budget, and therefore for measuring GRB radiative efficiency, for GRB 190114C.

3. Methodology

3.1. Data Reduction

We reduce the GBM data using a Python package, namely the Multi-Mission Maximum Likelihood Framework (Vianello et al. 2015). The data that we use for our spectral analysis include the two most strongly illuminated sodium iodide (NaI) scintillation detectors (n3, n4) and the most strongly illuminated bismuth germanium oxide (BGO) scintillation detector (b0) on board Fermi-GBM, as well as the corresponding response files (.rsp2 files are adopted). The detector selections are made by considering an angle of incidence less than 60° , for NaI, and the lowest angle of incidence, for BGO (Goldstein et al. 2012; Narayana Bhat et al. 2016). The Time-Tagged Event (TTE) data type is used for the NaI data (8 keV–1 MeV) and the BGO data (200 keV–40 MeV). To avoid the K-edge at 33.17 keV, the spectral energy range is also cut from 30 to 40 keV. The background fitting is chosen using two off-source intervals, including the pre-burst ($-20 \sim -10$ s) and post-burst (180 ~ 200 s) epochs, with the polynomial order being determined (0–4) by applying a likelihood ratio test. The source interval is selected over the duration ($-1 \sim 116$ s) reported by the Fermi-GBM team. The maximum likelihood-based statistics, the so-called Pgst, are used, given by a Poisson (observation)–Gaussian (background) profile likelihood (Cash 1979).

3.2. Bayesian Spectral Analysis

The spectral parameters are obtained by adopting a fully Bayesian analysis approach. The main idea is that after the experimental data are obtained, Bayes's theorem is applied to infer and update the probability distribution of a specific set of model parameters. After building up a Bayesian profile model (M), and given an observed data set (D), the posterior probability distribution $p(M|D)$ according to Bayes's theorem is given by

$$p(M|D) = \frac{p(D|M)p(M)}{p(D)}, \quad (2)$$

where $p(D|M)$ is the likelihood that combines the model and the observed data, expressing the probability of observing (or generating) the data set D from a given model M with its parameters; $p(M)$ is the prior on the model parameters; and $p(D)$ is called the evidence, which is a constant with the purpose of normalization. We utilize the typical spectral parameters

from the Fermi-GBM catalog as the prior distributions:

$$\left\{ \begin{array}{l} A_{\text{Band}} \sim \log \mathcal{N}(\mu = 0, \sigma = 2) \text{ cm}^{-2} \text{ keV}^{-1} \text{ s}^{-1} \\ \alpha_{\text{Band}} \sim \mathcal{N}(\mu = -1, \sigma = 0.5) \\ \beta_{\text{Band}} \sim \mathcal{N}(\mu = -2, \sigma = 0.5) \\ E_{\text{Band}} \sim \log \mathcal{N}(\mu = 2, \sigma = 1) \text{ keV} \\ A_{\text{CPL}} \sim \log \mathcal{N}(\mu = 0, \sigma = 2) \text{ cm}^{-2} \text{ keV}^{-1} \text{ s}^{-1} \\ \alpha_{\text{CPL}} \sim \mathcal{N}(\mu = -1, \sigma = 0.5) \\ E_{\text{CPL}} \sim \log \mathcal{N}(\mu = 2, \sigma = 1) \text{ keV} \\ A_{\text{BB}} \sim \log \mathcal{N}(\mu = -4, \sigma = 2) \text{ cm}^{-2} \text{ keV}^{-1} \text{ s}^{-1} \\ kT_{\text{BB}} \sim \log \mathcal{N}(\mu = 2, \sigma = 1) \text{ keV} \end{array} \right. \quad (3)$$

We employ a Markov Chain (MC) Monte Carlo sampling method (*emcee*; Foreman-Mackey et al. 2013) to sample the posterior. The parameter estimation is obtained at a maximum a posteriori probability from the Bayesian posterior density distribution, and its uncertainty (or the credible level) is evaluated from the Bayesian highest-posterior density interval at the 1σ (68%) Bayesian credible level.

3.3. Model Comparison

The best-fit model is reached by comparing the deviance information criterion (DIC) values of the different models and picking the one with the lowest value. The DIC is defined as $\text{DIC} = -2\log[p(\text{data}|\hat{\theta})] + 2p_{\text{DIC}}$, where $\hat{\theta}$ is the posterior mean of the parameters and p_{DIC} is the effective number of parameters. The preferred model is the one that provides the lowest DIC score. We report the Δ DIC values by comparing the best model with the other models in Table 1. Log(posterior) is adopted by the maximum likelihood ratio test method, which is treated as a reference for the model comparison (Vuong 1989).

3.4. BBlocks Methods

We use a method called Bayesian blocks (BBlocks; Scargle et al. 2013) to rebin the TTE light curves. The time bins are selected in such a way as to capture the true variability of the data. Such a calculation requires each bin to be consistent, with a constant Poisson rate. This allows for a variable time width and signal-to-noise ratio in each bin. As such, we first apply the BBlocks method with a false alarm probability $p_0 = 0.01$ to the TTE light curve of the most strongly illuminated GBM detector (n4). The other detectors (n3 and b0) are then binned into matching slices. We notice that the BBlocks analysis generates two slices (0.70 ~ 1.58 s and 1.58 ~ 1.71 s) from 0.70 to 1.71 s. On the other hand, the two slices have very high significance (263.97 and 115.59). To study the parameter evolution in great detail, we therefore rebin the time intervals with five narrower slices of significance >80 , instead. We also conduct the same analysis on the last slice of P_2 (5.51 ~ 5.69 s), generating two

narrower slices (5.51 ~ 5.65 s and 5.65 ~ 5.69 s), with significance >70 each, to study the temperature evolution in more detail. We therefore obtain 8 slices for P_1^{th} and 16 slices for P_2^{th} in order to study the photosphere properties.

4. Models

4.1. Deriving the Photosphere Properties Using the Traditional Method

The traditional method for deriving the photosphere properties invokes the standard fireball model (Mészáros & Rees 2000; Pe'er 2015; Zhang 2018). Within this framework, the fireball invokes thermally accelerated, matter-dominated, and finally shock-decelerated ejecta (Goodman 1986; Paczynski 1986).

The thermal emission of GRB 190114C is extremely strong, ranking second in its thermal-to-total flux ratio (21%) among the more than 2700 GRBs that have been observed by Fermi-GBM to date. The identification of the strong thermal component in GRB 190114C allows us to determine the physical properties of the relativistic outflow within the framework of the nondissipative photosphere theory (Pe'er et al. 2007; Vereshchagin & Aksenov 2017), which also applies to moderately dissipated photospheres where the photosphere spectrum is only mildly modified. The photosphere photons that are observed at a given time, corresponding to the one time bin in our time-resolved analysis, are assumed to be emitted from an independent thin shell. Therefore, the observed blackbody temperature kT_{obs} , the blackbody flux F_{BB} , and the total flux F_{tot} (thermal+nonthermal) of a given time bin determine the photosphere properties of the corresponding shell. The entire duration of the photosphere emission is conjugated by the emissions from a sequence of such shells. One can infer the bulk Lorentz factor Γ and the initial size of the flow R_0 in each time bin, as well as their temporal evolutions.

Within the framework of the standard fireball model (Pe'er et al. 2007), a given shell is generated at an initial radius

$$r_0(r_{\text{ph}} > r_s) = \frac{4^{3/2} d_L}{(1.48)^6 \xi^4 (1+z)^2} \left(\frac{F_{\text{BB}}^{\text{obs}}}{\mathbb{Y} F_{\text{tot}}^{\text{obs}}} \right)^{3/2} \mathfrak{R}, \quad (4)$$

and self-accelerates to reach a saturated Lorentz factor

$$\eta(\equiv \Gamma)(r_{\text{ph}} > r_s) = \left[\xi (1+z)^2 d_L \left(\frac{\mathbb{Y} F_{\text{tot}}^{\text{obs}} \sigma_T}{2m_p c^3 \mathfrak{R}} \right) \right]^{1/4} \quad (5)$$

in the coasting phase. If the photosphere radius is greater than the saturation radius, it reads

$$r_{\text{ph}}(>r_s) = \frac{L_0 \sigma_T}{8\pi m_p c^3 \Gamma^3}, \quad (6)$$

where the dimensionless parameter

$$\mathfrak{R} = \left(\frac{F_{\text{BB}}}{\sigma_B T^4} \right)^{1/2} = \xi \frac{(1+z)^2 r_{\text{ph}}}{d_L \Gamma} \quad (7)$$

presents the effective transverse size of the photosphere. The burst luminosity $L_0 = 4\pi d_L^2 \mathbb{Y} F_{\text{tot}}$ is given by the observation, while \mathbb{Y} is the ratio between the total fireball energy and the energy emitted in gamma rays. The numerical factor ξ is of the order of unity that can be obtained from angular integration. The luminosity distance d_L of the redshift z is integrated by

assuming the standard Friedmann–Lemaître–Robertson–Walker (FLRW) metric. Other physical constants are the Thomson cross section σ_T , the proton rest mass m_p , the speed of light c , and the Stefan–Boltzmann constant σ_B .

4.2. Directly Deriving the Fireball Properties from Observations

GRB 190114C has a redshift measurement. Its prompt emission is thermally subdominated and its light curve has a clear early pulse, indicating the afterglow initiation. These three properties mean that it is the first case where one can use observational properties to directly determine the fireball characteristics, including the dimensionless specific enthalpy at the engine η , the isotropic equivalent total mass M , the bulk Lorentz factor at the site of the photosphere Γ_{ph} , the initial afterglow Lorentz factor before the deceleration phase Γ_s , the kinetic energy in the fireball E_k , and the gamma-ray radiative efficiency η_γ . The method described below follows Zhang et al. (2021).

The initial total energy of a fireball is

$$E_{\text{tot}} = \eta M c^2. \quad (8)$$

The fireball undergoes rapid acceleration and reaches a Lorentz factor Γ_{ph} at the photosphere. The internal energy released as thermal emission can be estimated as

$$E_{\text{th}} = (\eta - \Gamma_{\text{ph}}) M c^2. \quad (9)$$

Afterward, the fireball moves at an almost constant speed, until the internal dissipation at the internal shocks occurs at a larger distance. The emitted nonthermal emission can be estimated as

$$E_{\text{nth}} = (\Gamma_{\text{ph}} - \Gamma_0) M c^2, \quad (10)$$

where Γ_s is the Lorentz factor after the dissipation and also the initial Lorentz factor in the afterglow phase.

The Lorentz factor at the photosphere radius Γ_{ph} can be estimated as (modified from Pe'er et al. 2007; Bégué & Iyyani 2014; see Zhang et al. 2021 for details)

$$\Gamma_{\text{ph}} = \left[(1+z)^2 D_L \frac{\mathcal{Y} \sigma_T F_\gamma^{\text{obs}}}{2m_p c^3 \mathcal{R}} \frac{\eta^{3/2}}{\eta - \Gamma_0} \right]^{2/9}, \quad (11)$$

$$\mathcal{R} = \left(\frac{F_{\text{BB}}^{\text{obs}}}{\sigma_B T^4} \right)^{1/2}.$$

which involves several direct observables, including the redshift z , the total flux F_γ^{obs} , the thermal flux $F_{\text{BB}}^{\text{obs}}$, and the observed temperature T . Other parameters are the pair multiplicity parameter \mathcal{Y} , which is commonly taken as 1; the luminosity distance D_L , computed from the redshift by adopting the FLRW cosmology; and fundamental constants, such as the speed of light c , the proton mass m_p , the Thomson cross section σ_T , and the Stefan–Boltzmann constant σ_B .

The initial Lorentz factor of the afterglow phase Γ_s can be derived by equating the kinetic energy to the swept up interstellar medium (ISM) mass at the deceleration time t_{dec} , which is an observable indicated by a light-curve pulse (the third pulse for 190114C). Using Equation (7.81) of

Table 2
Various Isotropic Energy Releases Were Observed by Different Satellite Instruments at Different Wavelengths and Different Time Intervals

Satellite-Instrument	$T_0+[t_{\text{start}}, t_{\text{stop}}]$ (s)	Observed Bandwidth	Isotropic Energy (erg)	Model (For Energy)	Reference
MAGIC ^a	$T_0+[62, 2454]$	0.3 ~ 1 TeV	$\sim 4.0 \times 10^{51}$	SPL	MAGIC Collaboration et al. (2019b)
Fermi-LAT ^b	$T_0+[2.1, 8000]$	0.1 ~ 10 GeV	$(1.09 \pm 0.24) \times 10^{53}$	SPL	This paper
Fermi-LAT ^b	$T_0+[2.1, 6]$	0.1 ~ 10 GeV	$(8.49 \pm 1.80) \times 10^{51}$	SPL	This paper
Fermi-LAT ^b	$T_0+[6, 8000]$	0.1 ~ 10 GeV	$(1.01 \pm 0.24) \times 10^{53}$	SPL	This paper
Fermi-GBM ^c	$T_0+[0, 116]$	0.001 ~ 10 MeV	$(2.82_{-0.25}^{+0.43}) \times 10^{53}$	(CPL+BB)/Band	This paper
Fermi-GBM ^c	$T_0+[0, 6]$...	$(2.29_{-0.09}^{+0.10}) \times 10^{53}$	CPL+BB	This paper
Fermi-GBM ^c	$T_0+[6, 116]$...	$(5.33_{-2.34}^{+4.23}) \times 10^{52}$	Band	This paper
Fermi-GBM ^c	$T_0+[0, 6]$...	$(3.69_{-0.67}^{+0.78}) \times 10^{52}$	CPL+BB	This paper
Fermi-GBM ^c	$T_0+[0, 6]$...	$(1.92_{-0.11}^{+0.12}) \times 10^{53}$	CPL+BB	This paper
Swift-XRT ^d	$T_0+[68, 1197626]$	0.3 ~ 10 KeV	$\sim 1.48 \times 10^{52}$	SPL	This paper

Notes.

^a Time-integrated isotropic equivalent energy releases observed by MAGIC from T_0+62 to T_0+2454 s, as reported by MAGIC Collaboration et al. (2019b).

^b Time-integrated isotropic equivalent energy releases from the Fermi-LAT observation with a (0.1–10 GeV) bandwidth, as well as those separated into prompt and afterglow emission, as defined in the methodology section.

^c Time-integrated isotropic equivalent energy releases from the Fermi-GBM observation, using the best models, as well as those separated into prompt and afterglow emission, and those separated into thermal and nonthermal energy releases, during the prompt emission phase.

^d The total isotropic equivalent energy release observed by Swift-XRT.

Zhang (2018) and the above arguments, we derive

$$\Gamma_s \simeq 170 t_{\text{dec},2}^{-3/8} \left(\frac{1+z}{2} \right)^{3/8} \left(\frac{E_{\text{th},52} + E_{\text{nth},52}}{n} \right)^{1/8} \left(\frac{\Gamma_0}{\eta - \Gamma_0} \right)^{1/8}, \quad (12)$$

where n is the ISM density, assumed as one particle per cubic centimeter, as usual.¹⁷

Simultaneously solving Equations (9)–(12), we obtain the fireball parameters η , Γ_{ph} , M , and Γ_s . In turn, we can calculate the kinetic energy of the afterglow

$$E_k = \Gamma_0 M c^2, \quad (13)$$

and the efficiency of the prompt gamma-ray emission

$$\eta_\gamma = \frac{E_{\text{th}} + E_{\text{nth}}}{E_{\text{tot}}} = \frac{\eta - \Gamma_0}{\eta}. \quad (14)$$

5. Results

5.1. Multiwavelength Observations

(1) TeV (MAGIC) Observations. The MAGIC telescopes observed for the first time a very-high-energy gamma-ray (>1 TeV) emission, from T_0+57 s to $T_0+15912$ s (MAGIC Collaboration et al. 2019b), setting the record for the highest photon energy to be detected from a GRB. Both the TeV light curve and spectrum can be well described by a PL model,¹⁸ with the temporal decay index $\hat{\alpha}_{\text{MAGIC}} = -1.60 \pm 0.07$ (Figure 3(a))

and the spectral decay index $\hat{\beta}_{\text{MAGIC}} = -2.16 \pm 0.30$ (Figure 3(b)). The total TeV-band (0.3–1 TeV) energy integrated between T_0+62 s and T_0+2454 s is $E_{\gamma,\text{iso}}^{\text{MAGIC}} \sim 4.0 \times 10^{51}$ erg (MAGIC Collaboration et al. 2019b).

(2) GeV (Fermi-LAT) Observations. The first GeV photon was observed by Fermi-LAT at $T_0+2.1$ s. The highest-energy photon detected by LAT is a 22.9 GeV event detected at T_0+15 s (Kocevski et al. 2019); therefore, this bandwidth (0.1–10 GeV) is reasonably adopted for measuring the total GeV energy detected by LAT. In Table 2, for comparison, we also report the results that are based on the other two bandwidths: (0.1–100 GeV) and (0.1–1 GeV). After that time, the light curve and spectrum as measured by LAT (0.1–10 GeV) from T_0+55 s to T_0+8000 s are well fitted by a PL model with a temporal decay index $\hat{\alpha}_{\text{LAT}} = -1.29 \pm 0.01$ (Figure 3(a)) and a spectral slope index $\hat{\beta}_{\text{LAT}} = -2.01 \pm 0.98$ (Figure 3(b)). The total GeV-band (0.1–10 GeV) energy integrated between $T_0+2.1$ s and T_0+8000 s is $E_{\gamma,\text{iso}}^{\text{LAT}} = (1.09 \pm 0.24) \times 10^{53}$ erg, which can be separated into two emission components: the prompt emission (≤ 6 s) accounts for $E_{\gamma,\text{iso}}^{\text{LAT}} = (8.49 \pm 1.80) \times 10^{51}$ erg, while the afterglow emission (>6 s) accounts for $E_{\gamma,\text{iso}}^{\text{LAT}} = (1.01 \pm 0.24) \times 10^{53}$ erg.

(3) MeV (Fermi-GBM) Observations. The duration of the GRB (T_{90}) is about 116 s, as reported by Fermi-GBM. The 1024 ms peak flux and the fluence at 10–1000 keV as measured by Fermi-GBM are 246.9 ± 0.9 photon $\text{cm}^{-2} \text{ s}^{-1}$ and $(4.436 \pm 0.005) \times 10^{-4}$ erg cm^{-2} , respectively. With a known redshift, $z = 0.4245 \pm 0.0005$ (Selsing et al. 2019), and based on the best models for each emission episode (the CPL+BB model for prompt emission and the Band model for afterglow emission), the total k -corrected isotropic energy in the rest-frame 1–10⁴ keV band as derived from the Fermi-GBM observations between T_0+0 s and T_0+116 s is $E_{\gamma,\text{iso}}^{\text{GBM}} = (2.82_{-0.25}^{+0.43}) \times 10^{53}$ erg (Wang et al. 2019b), while between T_0+15 s and T_0+25 s (P_3) it is $E_{\gamma,\text{iso}}^{\text{GBM}} \sim 1.24 \times 10^{52}$ erg. The prompt emission (≤ 6 s) accounts for $E_{\gamma,\text{iso}}^{\text{GBM}} = (2.29_{-0.09}^{+0.10}) \times 10^{53}$ erg, while the afterglow emission

¹⁷ Note that we do not discuss the case of a wind medium (Dai & Lu 1998; Mészáros et al. 1998; Chevalier & Li 1999) in our theoretical model (Zhang et al. 2021). This is because the afterglow observations suggest that the majority of GRBs, especially those with clear deceleration signatures, are consistent with a constant-density medium (Zhang et al. 2007; Liang et al. 2010). More importantly, for a wind medium, the fireball dynamics should be in the “thick shell” regime (Kobayashi & Zhang 2003; Wu et al. 2003), but because the observations do not require “thick shell” dynamics for this burst, we only consider a constant-density medium in our calculation.

¹⁸ The convention $E_{\nu,t} = t^{\hat{\alpha}} \nu^{\hat{\beta}}$ is adopted throughout the paper.

(>6 s) accounts for $E_{7,\text{iso}}^{\text{GBM}} = (5.33_{-2.34}^{+4.23}) \times 10^{52}$ erg. There is a ~ 3.24 s lag between the GBM emission and the LAT emission.

(4) keV (Swift-XRT) Observations. Following the trigger by Swift-BAT, the spacecraft slewed immediately to the location of the burst. The XRT began observing the afterglow at T_0+64 s. Pointed Windowed Timing mode data were collected from T_0+68 s to T_0+626 s, after which the count rate was low enough for Photon Counting mode to be utilized. The burst was followed for more than 28 days, although the last detection occurred on T_0+20 days. The XRT light curve showed a typical power-law behavior, with a power-law index $\hat{\alpha}_{\text{XRT}} = -1.39 + 0.01$ (Figure 3). The isotropic X-ray energy release $E_{X,\text{iso}}^{\text{XRT}}$ measured by Swift-XRT (0.3–10 keV) from T_0+68 s to $T_0+13.86$ days is $\sim 1.48 \times 10^{52}$ erg.

(5) Optical Observations. Optical data have been gathered from literature references (MAGIC Collaboration et al. 2019b; Misra et al. 2021; Jordana-Mitjans et al. 2020; Melandri et al. 2022), as have the Gamma-Ray Coordinates Network data (Bikmaev et al. 2019; Im et al. 2019a, 2019b; Kim & Im 2019; Kim et al. 2019; Mazaeva et al. 2019; Watson et al. 2019a, 2019b). The automatically processed UVOT data have also been used. All afterglow data have been host-subtracted, using the host galaxy values taken from de Ugarte Postigo et al. (2020), and only late data without any supernova contributions have been used. Note that Jordana-Mitjans et al. (2020) found chromatic evolution in their early RINGO3 data. However, this effect is small, leading to some additional scatter around the first and second steep-to-shallow decay transitions. After the respective host galaxy magnitude has been subtracted from each band, all the bands are shifted to the R_c band, to produce a composite light curve stretching from 33 s to 56.4 days after the GRB trigger. The light curve can be described by multiple power-law decay segments, in a steep–normal–shallow–normal–steep arrangement. The first two segments have slopes $\hat{\alpha}_{\text{opt},1} = -1.628 \pm 0.012$ and $\hat{\alpha}_{\text{opt},2} = -1.035 \pm 0.006$, with a break time at $t_{b,1} = 429 \pm 61$ s and a sharp transition index with $n = -13.3 \pm 2.0$ (Figure 3(a)). Such an early steep–normal transition is consistent with the superposition of a reverse shock component with a forward shock component. After a second sharp break ($n = -8.6 \pm 1.9$) at $t_{b,2} = 4856 \pm 216$ s, the light curve goes into an even flatter phase, decaying with $\hat{\alpha}_{\text{opt},3} = -0.512 \pm 0.035$. At a break time $t_{b,3} = 0.548 \pm 0.036$ days (with a smoother transition index $n = 4.4 \pm 2.1$), the decay becomes steeper again, reaching a value similar to $\hat{\alpha}_{\text{opt},2}$, $\hat{\alpha}_{\text{opt},4} = -1.146 \pm 0.036$, indicating that the shallow decay phase may be interpreted as an energy injection. We find a final break at $t_{b,4} = 6.33 \pm 1.26$ days, to an even steeper decay $\hat{\alpha}_{\text{opt},5} = -1.714 \pm 0.041$ ($n = 10$ had to be fixed).

This final break may represent a jet break. If so, the post-break slope would be quite shallow, but this would not be unprecedented (see the sample in Zeh et al. 2006 for comparison). There is no conclusive evidence from the X-ray data for this break. However, we note that the final three Swift data points are decaying more steeply than before, while the X-ray data only extends to ≈ 14 days, which does not allow strong conclusions to be drawn.

(6) Radio Observations. The radio data points are taken from Laskar et al. (2019). Radio observations were carried out by the Atacama Large Millimeter/submillimeter Array (ALMA) in Band 3, with a center frequency of 97.5 GHz, spanning the period from $T_0+0.0995$ days to $T_0+0.217$ days and lasting for

3 hr, and can be used alongside the NSF’s Karl G. Jansky VLA observations—a full sequence of observations spanning 5–38 GHz, starting at $T_0+0.197$ days and ending at $T_0+0.261$ days. As shown in the left panel of Figure 3, the radio afterglow light curve from the ALMA observations is well fitted with a PL model, with a temporal decay index $\hat{\alpha}_{\text{radio}} = -0.69 \pm 0.02$. The radio observations at $\lesssim T_0+0.03$ days, as well as the optical and millimeter observations, were interpreted as emissions from the reverse-shocked ejecta in Laskar et al. (2019).

5.2. Time-integrated and Time-resolved Spectral Analysis

We first perform a time-integrated spectral analysis (treating the entire T_{90} as one time bin, i.e., from T_0 to $T_0 + 116$ s) by using various GRB spectral models, including power-law (PL), blackbody (BB), cutoff power-law (CPL), Band function (Band et al. 1993), smoothly broken power-law (SBKPL), PL+BB (Ryde 2005), PL+Bandcut, CPL+BB (Li 2019b), and Band+BB (Guiriec et al. 2011) models, respectively. Our refined time-integrated spectral analysis suggests that the CPL+BB model can best characterize the spectral shape of the burst. The corresponding corner plot is shown in Figure 4.

GRB spectra are known to evolve over different pulses, or even within a pulse. The time-integrated spectral analysis, therefore, must be replaced by a time-resolved spectral analysis in order to study the GRB radiation mechanism in great detail. We next perform a time-resolved spectral analysis for the Fermi-GBM observations. Thanks to its high fluence of $(4.436 \pm 0.005) \times 10^{-4}$ erg cm $^{-2}$, the fifth-highest-fluence GRB ever observed by Fermi-GBM, we are able to divide its T_{90} duration (116 s) into 48 slices, with each time bin containing enough photons to conduct a high-significance spectral analysis. We use the typical GRB spectral model, the Band model (Band et al. 1993), to fit the time-resolved spectra in each slice (see Table 3). We find that the low-energy photon index α exhibits a widespread temporal variability (-0.14 to -1.99), and that the majority of the α values in the first two pulses are harder than the typical value of α defined by the synchrotron line of death ($\alpha = -2/3$; Preece et al. 1998), suggesting a significant contribution from thermal emission from the fireball photosphere (Mészáros & Rees 2000; Ryde et al. 2010). The majority of the high-energy photon index β values are not well constrained, indicating that the CPL model is preferred in comparison to the Band model (Table 3). The violation of the synchrotron limit encourages us to search for an additional thermal component. To search for the best model for characterizing the spectral shape of the burst, we attempt to fit the time-resolved spectra in each slice with both the CPL and the CPL+BB models. The DIC of the CPL+BB model is at least 10 and can be hundreds less than that of the CPL model, indicating that adding a thermal component improves the spectral fitting greatly ($\Delta\text{DIC} > 10$; Acuner et al. 2020). The CPL+BB model (Ryde 2005; Battelino et al. 2007) gives a better fit in comparison to the CPL (see Table 4), Band, and other models, from $T_0+0.55$ s to $T_0+1.93$ s in P_1 (including eight slices; hereafter, P_1^{th}) and from $T_0+2.45$ s to $T_0+5.69$ s in P_2 (including 16 slices; hereafter, P_2^{th}), based on the DIC. P_1^{th} and P_2^{th} correspond to the peak fluxes of P_1 and P_2 , respectively, which correspond precisely to the epochs when the power-law indices α of the single CPL fits are beyond the limits of the synchrotron line of death (Preece et al. 1998), i.e., $\alpha > -2/3$, indicating the existence of a thermal component

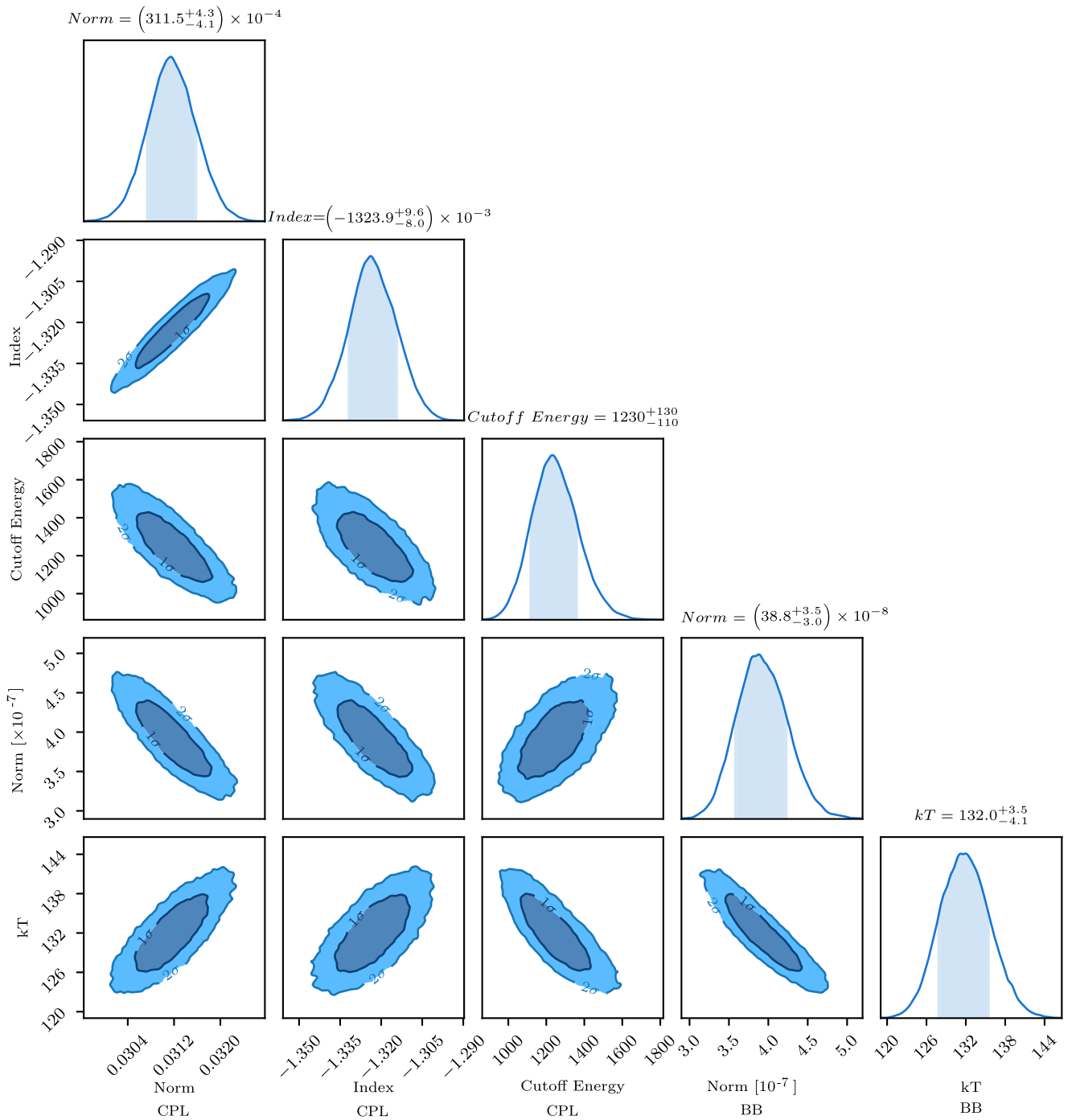


Figure 4. Bayesian MC time-integrated spectral fits for the Fermi-GBM data (from 0 s to 116 s; T_{90} duration). We apply 20 chains, with each chain iterating 10^4 times and burning the first 10^3 times. The parameters are the normalization (Norm CPL), cutoff energy, and power-law index of the CPL model, as well as the normalization (Norm BB) and temperature (kT) of the BB model.

(Ryde 2004; Ghirlanda et al. 2007). An example of a νF_ν spectrum for one time slice (4.95–5.45 s) with the CPL+BB model giving the best fit is displayed in Figure 5. Both P_1 and P_2 include nonthermal and subdominant thermal components. The thermal components observed in GRB 190114C exhibit pulse-wise temporal properties, i.e., those in P_1 and P_2 evolve independently over their pulse durations (Figure 6). Such a feature provides a unique opportunity to study the photosphere properties at distinctly different epochs of central engine activities.

The time-resolved analysis shows that almost all the low-energy photon index α values of the CPL-only fits in P_{A0} are much softer than those in P_1 and P_2 (Figure 1), suggesting that the emission has a different origin. The index α gradually decreases toward -2 , a typical value for synchrotron radiation, which indicates that the fireball has entered the afterglow phase. We set the beginning of the epoch as the deceleration time when the mass of the ambient medium collected by the shockwave is comparable to $1/\Gamma$ of the fireball energy (Meszaros & Rees 1993; Sari & Piran 1999).

Table 3
Time-resolved Spectral Fit Results of GRB 190114C

$t_{\text{start}} \sim t_{\text{stop}}$ (1)	S (2)	K (3)	α (4)	E_c (5)	F (6)	K (7)	α (8)	β (9)	E_p (10)	F (11)	ΔDIC (12)	$p_{\text{DIC,CPL}}$ (13)	$p_{\text{DIC,Band}}$ (14)
P_1													
−0.067~0.029	8.40	$0.37_{-0.07}^{+0.07} \times 10^{-1}$	$-0.98_{-0.17}^{+0.17}$	891_{-519}^{+616}	$4.68_{-2.45}^{+4.85} \times 10^{-6}$	$0.37_{-0.08}^{+0.08} \times 10^{-1}$	$-0.98_{-0.19}^{+0.19}$	$-6.17_{-2.71}^{+2.72}$	921_{-501}^{+614}	$4.42_{-1.99}^{+4.94} \times 10^{-6}$	0.0	0.5	0.3
0.029~0.141	21.45	$134.00_{-38.70}^{+38.90} \times 10^{-1}$	$-1.11_{-0.08}^{+0.08}$	1170_{-479}^{+517}	$10.37_{-4.94}^{+10.65} \times 10^{-6}$	$0.71_{-0.05}^{+0.05} \times 10^{-1}$	$-1.15_{-0.07}^{+0.06}$	$-5.12_{-3.12}^{+2.74}$	1211_{-370}^{+386}	$12.53_{-3.19}^{+3.27} \times 10^{-6}$	81.7	0.6	1.4
0.141~0.294	39.83	$1.41_{-0.08}^{+0.08} \times 10^{-1}$	$-1.11_{-0.05}^{+0.05}$	944_{-232}^{+230}	$16.99_{-3.33}^{+5.07} \times 10^{-6}$	$1.41_{-0.08}^{+0.08} \times 10^{-1}$	$-1.11_{-0.05}^{+0.05}$	$-6.34_{-2.54}^{+2.50}$	824_{-165}^{+165}	$17.33_{-2.84}^{+3.78} \times 10^{-6}$	0.3	2.6	2.8
0.294~0.415	50.05	$2.78_{-0.17}^{+0.17} \times 10^{-1}$	$-0.90_{-0.05}^{+0.05}$	451_{-66}^{+65}	$21.90_{-3.63}^{+4.86} \times 10^{-6}$	$2.78_{-0.18}^{+0.18} \times 10^{-1}$	$-0.90_{-0.05}^{+0.05}$	$-5.92_{-2.72}^{+2.68}$	492_{-56}^{+55}	$22.58_{-3.11}^{+3.64} \times 10^{-6}$	0.0	2.8	2.9
0.415~0.546	73.35	$4.42_{-0.18}^{+0.18} \times 10^{-1}$	$-0.78_{-0.04}^{+0.04}$	452_{-42}^{+42}	$40.15_{-5.07}^{+5.55} \times 10^{-6}$	$4.44_{-0.18}^{+0.18} \times 10^{-1}$	$-0.78_{-0.04}^{+0.04}$	$-6.21_{-2.57}^{+2.53}$	545_{-40}^{+39}	$41.10_{-3.84}^{+4.81} \times 10^{-6}$	−0.0	2.9	3.0
0.546~0.701	96.49	$6.47_{-0.22}^{+0.22} \times 10^{-1}$	$-0.66_{-0.03}^{+0.03}$	354_{-23}^{+23}	$49.72_{-5.02}^{+5.44} \times 10^{-6}$	$6.63_{-0.26}^{+0.26} \times 10^{-1}$	$-0.65_{-0.03}^{+0.04}$	$-4.05_{-1.89}^{+1.24}$	454_{-26}^{+25}	$54.13_{-5.79}^{+6.04} \times 10^{-6}$	−6.0	2.9	0.8
0.701~1.579	263.62	$7.71_{-0.08}^{+0.08} \times 10^{-1}$	$-0.68_{-0.01}^{+0.01}$	451_{-11}^{+10}	$80.76_{-2.94}^{+3.02} \times 10^{-6}$	$7.72_{-0.08}^{+0.08} \times 10^{-1}$	$-0.68_{-0.01}^{+0.01}$	$-6.43_{-2.31}^{+1.96}$	594_{-10}^{+10}	$81.07_{-1.95}^{+2.16} \times 10^{-6}$	−1.1	3.0	2.6
1.579~1.713	117.21	$8.32_{-0.16}^{+0.16} \times 10^{-1}$	$-0.47_{-0.02}^{+0.02}$	515_{-22}^{+22}	$147.00_{-11.77}^{+12.37} \times 10^{-6}$	$8.32_{-0.17}^{+0.16} \times 10^{-1}$	$-0.46_{-0.02}^{+0.02}$	$-6.73_{-2.14}^{+2.01}$	788_{-25}^{+25}	$146.90_{-8.28}^{+9.38} \times 10^{-6}$	−0.1	3.0	3.0
1.713~1.805	88.47	$8.93_{-0.34}^{+0.34} \times 10^{-1}$	$-0.56_{-0.04}^{+0.04}$	319_{-21}^{+21}	$67.00_{-6.55}^{+8.01} \times 10^{-6}$	$9.12_{-0.42}^{+0.41} \times 10^{-1}$	$-0.54_{-0.04}^{+0.04}$	$-5.38_{-2.98}^{+2.41}$	447_{-27}^{+26}	$70.25_{-7.62}^{+10.60} \times 10^{-6}$	−1.9	2.9	1.9
1.805~1.933	80.82	$6.01_{-0.33}^{+0.33} \times 10^{-1}$	$-0.84_{-0.04}^{+0.04}$	275_{-26}^{+26}	$28.49_{-3.22}^{+3.60} \times 10^{-6}$	$9.62_{-1.71}^{+1.71} \times 10^{-1}$	$-0.57_{-0.11}^{+0.11}$	$-2.15_{-0.09}^{+0.10}$	199_{-27}^{+27}	$42.18_{-9.59}^{+14.55} \times 10^{-6}$	−20.9	2.9	0.5
1.933~2.137	72.22	$3.10_{-0.16}^{+0.16} \times 10^{-1}$	$-1.01_{-0.04}^{+0.04}$	392_{-46}^{+46}	$18.98_{-2.28}^{+2.76} \times 10^{-6}$	$3.11_{-0.16}^{+0.16} \times 10^{-1}$	$-1.01_{-0.04}^{+0.04}$	$-6.43_{-2.36}^{+2.35}$	381_{-32}^{+32}	$19.17_{-1.81}^{+2.09} \times 10^{-6}$	0.4	2.9	3.1
2.137~2.406	63.87	$2.48_{-0.16}^{+0.16} \times 10^{-1}$	$-1.00_{-0.04}^{+0.05}$	301_{-36}^{+36}	$11.75_{-1.52}^{+1.70} \times 10^{-6}$	$2.49_{-0.17}^{+0.17} \times 10^{-1}$	$-1.00_{-0.05}^{+0.05}$	$-6.41_{-2.41}^{+2.39}$	297_{-26}^{+25}	$11.82_{-1.24}^{+1.54} \times 10^{-6}$	0.5	2.8	3.1
2.406~2.452	37.17	$2.83_{-0.19}^{+0.19} \times 10^{-1}$	$-1.01_{-0.06}^{+0.06}$	1040_{-291}^{+285}	$42.69_{-10.96}^{+18.09} \times 10^{-6}$	$2.90_{-0.21}^{+0.21} \times 10^{-1}$	$-1.00_{-0.07}^{+0.07}$	$-4.30_{-3.02}^{+2.00}$	916_{-210}^{+225}	$45.91_{-10.74}^{+15.24} \times 10^{-6}$	−3.8	2.3	1.0
P_2													
2.452~2.642	152.49	$9.41_{-0.14}^{+0.14} \times 10^{-1}$	$-0.35_{-0.02}^{+0.02}$	464_{-15}^{+15}	$169.90_{-10.59}^{+11.71} \times 10^{-6}$	$9.43_{-0.14}^{+0.14} \times 10^{-1}$	$-0.35_{-0.02}^{+0.02}$	$-6.95_{-2.08}^{+1.98}$	763_{-18}^{+17}	$170.30_{-6.92}^{+8.70} \times 10^{-6}$	−0.2	3.0	2.9
2.642~2.882	135.79	$6.40_{-0.10}^{+0.10} \times 10^{-1}$	$-0.51_{-0.02}^{+0.02}$	559_{-22}^{+22}	$117.20_{-7.44}^{+8.53} \times 10^{-6}$	$6.41_{-0.10}^{+0.10} \times 10^{-1}$	$-0.51_{-0.02}^{+0.02}$	$-5.55_{-2.30}^{+1.68}$	827_{-23}^{+24}	$118.90_{-5.62}^{+6.59} \times 10^{-6}$	−2.4	3.0	2.4
2.882~3.088	102.21	$4.47_{-0.09}^{+0.09} \times 10^{-1}$	$-0.53_{-0.02}^{+0.02}$	666_{-33}^{+33}	$102.80_{-8.80}^{+9.27} \times 10^{-6}$	$4.47_{-0.09}^{+0.09} \times 10^{-1}$	$-0.53_{-0.02}^{+0.02}$	$-5.93_{-2.47}^{+1.99}$	974_{-37}^{+37}	$103.50_{-5.88}^{+6.94} \times 10^{-6}$	−1.2	3.0	2.5
3.088~3.208	92.58	$4.99_{-0.11}^{+0.11} \times 10^{-1}$	$-0.45_{-0.03}^{+0.03}$	814_{-50}^{+50}	$180.70_{-18.31}^{+22.92} \times 10^{-6}$	$5.16_{-0.12}^{+0.12} \times 10^{-1}$	$-0.39_{-0.03}^{+0.03}$	$-2.85_{-0.13}^{+0.13}$	1099_{-49}^{+49}	$192.00_{-15.55}^{+16.16} \times 10^{-6}$	−53.8	3.0	4.0
3.208~3.605	147.68	$4.58_{-0.06}^{+0.06} \times 10^{-1}$	$-0.35_{-0.02}^{+0.02}$	619_{-20}^{+20}	$131.60_{-10.15}^{+10.15} \times 10^{-6}$	$4.64_{-0.07}^{+0.06} \times 10^{-1}$	$-0.33_{-0.02}^{+0.02}$	$-2.88_{-0.09}^{+0.09}$	968_{-24}^{+24}	$149.00_{-7.26}^{+7.72} \times 10^{-6}$	−93.1	3.0	4.0
3.605~3.739	80.43	$4.00_{-0.10}^{+0.10} \times 10^{-1}$	$-0.32_{-0.04}^{+0.04}$	594_{-36}^{+36}	$115.80_{-14.13}^{+15.62} \times 10^{-6}$	$4.04_{-0.10}^{+0.10} \times 10^{-1}$	$-0.30_{-0.04}^{+0.04}$	$-3.06_{-0.20}^{+0.21}$	966_{-42}^{+42}	$129.30_{-11.48}^{+12.41} \times 10^{-6}$	−19.7	2.9	3.9
3.739~3.959	140.01	$6.34_{-0.10}^{+0.10} \times 10^{-1}$	$-0.20_{-0.02}^{+0.02}$	533_{-19}^{+19}	$193.50_{-14.73}^{+15.29} \times 10^{-6}$	$6.55_{-0.11}^{+0.11} \times 10^{-1}$	$-0.14_{-0.03}^{+0.03}$	$-2.71_{-0.07}^{+0.07}$	873_{-23}^{+23}	$224.70_{-13.54}^{+13.46} \times 10^{-6}$	−170.4	3.0	4.0
3.959~4.096	129.78	$9.68_{-0.18}^{+0.18} \times 10^{-1}$	$-0.19_{-0.03}^{+0.03}$	399_{-14}^{+14}			$-0.19_{-0.03}^{+0.03}$	$-3.65_{-0.23}^{+0.35}$	709_{-19}^{+19}		−11.0	3.0	3.8

G

Table 3
(Continued)

$t_{\text{start}} \sim t_{\text{stop}}$ (1)	S (2)	K (3)	α (4)	E_c (5)	F (6)	K (7)	α (8)	β (9)	E_p (10)	F (11)	ΔDIC (12)	$P_{\text{DIC,CPL}}$ (13)	$P_{\text{DIC,Band}}$ (14)
4.096~4.442	171.47	$8.48_{-0.13}^{+0.13} \times 10^{-1}$	$-0.44_{-0.02}^{+0.02}$	365_{-11}^{+11}	$175.70_{-12.87}^{+14.96} \times 10^{-6}$	$9.75_{-0.19}^{+0.19} \times 10^{-1}$	$-0.44_{-0.02}^{+0.02}$	$-3.60_{-0.21}^{+0.39}$	560_{-13}^{+13}	$187.10_{-10.94}^{+12.17} \times 10^{-6}$	-9.2	3.0	3.5
4.442~4.509	67.63	$7.06_{-0.34}^{+0.35} \times 10^{-1}$	$-0.73_{-0.04}^{+0.04}$	350_{-33}^{+32}	$49.84_{-6.25}^{+7.13} \times 10^{-6}$	$7.07_{-0.36}^{+0.35} \times 10^{-1}$	$-0.73_{-0.05}^{+0.05}$	$-5.87_{-2.78}^{+2.69}$	440_{-30}^{+30}	$51.28_{-5.57}^{+6.70} \times 10^{-6}$	-0.4	2.9	2.8
4.509~4.770	142.78	$7.16_{-0.12}^{+0.12} \times 10^{-1}$	$-0.65_{-0.02}^{+0.02}$	493_{-20}^{+20}	$88.02_{-5.44}^{+5.56} \times 10^{-6}$	$7.16_{-0.12}^{+0.12} \times 10^{-1}$	$-0.65_{-0.02}^{+0.02}$	$-6.78_{-2.13}^{+2.03}$	666_{-19}^{+19}	$88.41_{-3.73}^{+4.12} \times 10^{-6}$	0.0	3.0	3.1
4.770~4.950	134.52	$9.70_{-0.21}^{+0.21} \times 10^{-1}$	$-0.45_{-0.02}^{+0.02}$	351_{-14}^{+14}	$96.19_{-6.45}^{+6.57} \times 10^{-6}$	$9.70_{-0.20}^{+0.20} \times 10^{-1}$	$-0.45_{-0.02}^{+0.02}$	$-7.33_{-1.84}^{+1.86}$	542_{-14}^{+14}	$96.30_{-4.29}^{+4.52} \times 10^{-6}$	0.6	3.0	3.2
4.950~5.451	184.67	$6.94_{-0.10}^{+0.10} \times 10^{-1}$	$-0.62_{-0.02}^{+0.02}$	422_{-13}^{+13}	$72.22_{-3.51}^{+3.53} \times 10^{-6}$	$6.94_{-0.10}^{+0.10} \times 10^{-1}$	$-0.62_{-0.01}^{+0.01}$	$-6.97_{-2.05}^{+1.97}$	582_{-12}^{+12}	$72.22_{-2.36}^{+2.46} \times 10^{-6}$	0.1	3.0	3.1
5.451~5.514	77.55	$10.10_{-0.41}^{+0.41} \times 10^{-1}$	$-0.42_{-0.04}^{+0.04}$	302_{-20}^{+20}	$83.08_{-9.34}^{+10.90} \times 10^{-6}$	$10.12_{-0.40}^{+0.40} \times 10^{-1}$	$-0.41_{-0.04}^{+0.04}$	$-6.81_{-2.15}^{+2.16}$	475_{-21}^{+21}	$83.12_{-6.74}^{+6.69} \times 10^{-6}$	0.5	2.9	3.2
5.514~5.689	109.97	$10.10_{-0.43}^{+0.43} \times 10^{-1}$	$-0.55_{-0.03}^{+0.03}$	193_{-10}^{+10}	$37.07_{-3.20}^{+3.57} \times 10^{-6}$	$10.49_{-0.57}^{+0.58} \times 10^{-1}$	$-0.53_{-0.04}^{+0.04}$	$-4.13_{-1.47}^{+1.15}$	270_{-12}^{+12}	$39.58_{-4.22}^{+4.51} \times 10^{-6}$	-5.6	2.9	1.1
5.689~5.808	69.83	$6.33_{-0.59}^{+0.59} \times 10^{-1}$	$-0.89_{-0.06}^{+0.06}$	171_{-20}^{+20}	$17.29_{-2.54}^{+3.08} \times 10^{-6}$	$5.15_{-0.21}^{+0.21} \times 10^{-1}$	$-1.00_{-0.04}^{+0.04}$	$-5.10_{-3.08}^{+2.35}$	226_{-5}^{+5}	$19.52_{-1.50}^{+2.96} \times 10^{-6}$	2.1	2.6	0.9
5.808~6.000	60.35	$2.46_{-0.32}^{+0.32} \times 10^{-1}$	$-1.35_{-0.08}^{+0.07}$	202_{-41}^{+41}	$8.22_{-1.45}^{+1.64} \times 10^{-6}$	$4.53_{-1.15}^{+1.21} \times 10^{-1}$	$-1.06_{-0.13}^{+0.13}$	$-2.20_{-0.11}^{+0.11}$	83_{-11}^{+11}	$11.53_{-3.72}^{+5.05} \times 10^{-6}$	-18.9	1.6	-0.6
P_{AO}													
6.000~6.436	62.10	$1.02_{-0.11}^{+0.10} \times 10^{-1}$	$-1.63_{-0.06}^{+0.06}$	440_{-138}^{+133}	$5.80_{-0.88}^{+1.17} \times 10^{-6}$	$1.09_{-0.16}^{+0.14} \times 10^{-1}$	$-1.60_{-0.08}^{+0.07}$	$-5.13_{-3.31}^{+2.87}$	139_{-32}^{+29}	$5.98_{-1.32}^{+2.08} \times 10^{-6}$	-2.0	1.0	0.1
6.436~6.867	50.89	$0.71_{-0.07}^{+0.07} \times 10^{-1}$	$-1.73_{-0.05}^{+0.05}$	537_{-182}^{+201}	$4.66_{-0.66}^{+0.85} \times 10^{-6}$	$0.88_{-0.20}^{+0.14} \times 10^{-1}$	$-1.64_{-0.11}^{+0.10}$	$-3.58_{-2.81}^{+1.50}$	113_{-40}^{+33}	$5.21_{-1.58}^{+2.31} \times 10^{-6}$	-19.6	1.4	-15.2
6.867~8.221	64.64	$0.44_{-0.01}^{+0.01} \times 10^{-1}$	$-1.77_{-0.02}^{+0.02}$	892_{-86}^{+84}	$3.55_{-0.15}^{+0.14} \times 10^{-6}$	$0.43_{-0.05}^{+0.02} \times 10^{-1}$	$-1.81_{-0.05}^{+-0.00}$	$-4.96_{-2.72}^{+2.68}$	630_{-265}^{+275}	$4.75_{-0.81}^{+0.43} \times 10^{-6}$	-31.8	2.2	-23.1
8.221~9.567	49.76	$0.32_{-0.01}^{+0.01} \times 10^{-1}$	$-1.78_{-0.03}^{+0.03}$	830_{-140}^{+132}	$2.59_{-0.17}^{+0.14} \times 10^{-6}$	$0.29_{-0.01}^{+0.01} \times 10^{-1}$	$-1.85_{-0.03}^{+0.02}$	$-5.02_{-2.64}^{+2.64}$	647_{-275}^{+264}	$3.50_{-0.37}^{+0.22} \times 10^{-6}$	-6.2	2.2	1.5
9.567~12.400	54.86	$0.22_{-0.01}^{+0.01} \times 10^{-1}$	$-1.86_{-0.03}^{+0.03}$	706_{-192}^{+193}	$1.83_{-0.16}^{+0.17} \times 10^{-6}$	$0.21_{-0.02}^{+0.02} \times 10^{-1}$	$-1.91_{-0.05}^{+0.06}$	$-5.15_{-2.54}^{+2.52}$	305_{-221}^{+362}	$2.33_{-0.52}^{+0.43} \times 10^{-6}$	-7.6	2.1	-6.5
12.400~15.547	47.53	$0.17_{-0.01}^{+0.01} \times 10^{-1}$	$-1.93_{-0.03}^{+0.03}$	699_{-205}^{+207}	$1.47_{-0.14}^{+0.14} \times 10^{-6}$	$0.15_{-0.00}^{+0.00} \times 10^{-1}$	$-1.99_{-0.01}^{+0.01}$	$-5.54_{-2.31}^{+2.37}$	512_{-312}^{+321}	$2.11_{-0.09}^{+0.06} \times 10^{-6}$	0.3	2.0	1.0
P_3													
15.547~15.872	38.28	$0.74_{-0.07}^{+0.07} \times 10^{-1}$	$-1.49_{-0.06}^{+0.06}$	552_{-182}^{+199}	$4.59_{-0.93}^{+1.03} \times 10^{-6}$	$0.76_{-0.10}^{+0.09} \times 10^{-1}$	$-1.47_{-0.08}^{+0.08}$	$-5.07_{-2.62}^{+2.60}$	278_{-90}^{+76}	$4.77_{-0.98}^{+1.65} \times 10^{-6}$	-1.8	1.7	0.0
15.872~16.173	49.52	$1.06_{-0.09}^{+0.09} \times 10^{-1}$	$-1.49_{-0.06}^{+0.05}$	649_{-214}^{+197}	$6.94_{-1.13}^{+1.74} \times 10^{-6}$	$1.14_{-0.08}^{+0.08} \times 10^{-1}$	$-1.45_{-0.05}^{+0.05}$	$-6.18_{-2.61}^{+2.61}$	248_{-31}^{+32}	$6.59_{-0.76}^{+0.74} \times 10^{-6}$	0.5	1.7	2.4
16.173~16.927	98.83	$1.99_{-0.14}^{+0.14} \times 10^{-1}$	$-1.39_{-0.04}^{+0.04}$	198_{-23}^{+23}	$6.71_{-0.64}^{+0.78} \times 10^{-6}$	$2.94_{-0.38}^{+0.38} \times 10^{-1}$	$-1.20_{-0.07}^{+0.07}$	$-2.36_{-0.08}^{+0.09}$	88_{-7}^{+7}	$8.23_{-1.38}^{+1.70} \times 10^{-6}$	-18.7	2.6	3.1
16.927~17.324	59.55	$1.19_{-0.14}^{+0.14} \times 10^{-1}$	$-1.59_{-0.06}^{+0.07}$	245_{-56}^{+53}	$5.11_{-0.77}^{+0.96} \times 10^{-6}$	$1.23_{-0.16}^{+0.16} \times 10^{-1}$	$-1.57_{-0.07}^{+0.07}$	$-5.79_{-2.80}^{+2.79}$	96_{-10}^{+10}	$5.23_{-0.93}^{+1.19} \times 10^{-6}$	0.7	1.7	2.5

Table 3
(Continued)

$t_{\text{start}} \sim t_{\text{stop}}$ (1)	S (2)	K (3)	α (4)	E_c (5)	F (6)	K (7)	α (8)	β (9)	E_p (10)	F (11)	ΔDIC (12)	$p_{\text{DIC,CPL}}$ (13)	$p_{\text{DIC,Band}}$ (14)
17.324~17.719	51.00	$0.86^{+0.12}_{-0.12} \times 10^{-1}$	$-1.69^{+0.07}_{-0.07}$	283^{+83}_{-87}	$4.31^{+0.94}_{-0.74} \times 10^{-6}$	$1.00^{+0.17}_{-0.16} \times 10^{-1}$	$-1.62^{+0.08}_{-0.08}$	$-3.45^{+1.21}_{-2.00}$	70^{+11}_{-10}	$4.57^{+1.54}_{-1.06} \times 10^{-6}$	-5.3	-0.1	-1.2
17.719~20.397	95.90	$0.64^{+0.04}_{-0.04} \times 10^{-1}$	$-1.72^{+0.04}_{-0.03}$	210^{+26}_{-27}	$3.04^{+0.29}_{-0.28} \times 10^{-6}$	$0.77^{+0.10}_{-0.10} \times 10^{-1}$	$-1.63^{+0.06}_{-0.06}$	$-2.86^{+0.48}_{-0.09}$	53^{+4}_{-4}	$3.27^{+0.77}_{-0.59} \times 10^{-6}$	-14.2	2.5	-3.3
20.397~21.699	50.58	$0.34^{+0.03}_{-0.03} \times 10^{-1}$	$-1.95^{+0.04}_{-0.04}$	197^{+36}_{-37}	$2.32^{+0.29}_{-0.26} \times 10^{-6}$	$0.64^{+0.13}_{-0.12} \times 10^{-1}$	$-1.65^{+0.08}_{-0.08}$	$-3.21^{+0.67}_{-0.11}$	31^{+1}_{-1}	$2.11^{+0.68}_{-0.55} \times 10^{-6}$	6.0	1.7	-2.4
21.699~23.330	37.70	$0.21^{+0.02}_{-0.02} \times 10^{-1}$	$-1.96^{+0.04}_{-0.04}$	240^{+51}_{-53}	$1.49^{+0.18}_{-0.16} \times 10^{-6}$	$0.27^{+0.06}_{-0.06} \times 10^{-1}$	$-1.85^{+0.09}_{-0.08}$	$-4.14^{+1.83}_{-2.89}$	17^{+5}_{-5}	$1.55^{+0.71}_{-0.62} \times 10^{-6}$	-8.1	1.7	-7.0
23.330~26.530	39.21	$0.14^{+0.02}_{-0.02} \times 10^{-1}$	$-1.91^{+0.06}_{-0.06}$	347^{+122}_{-113}	$1.04^{+0.18}_{-0.14} \times 10^{-6}$	$0.19^{+0.05}_{-0.05} \times 10^{-1}$	$-1.82^{+0.12}_{-0.10}$	$-4.78^{+2.52}_{-2.73}$	31^{+8}_{-8}	$1.04^{+0.52}_{-0.39} \times 10^{-6}$	-6.9	1.2	-5.5
26.530~33.075	37.67	$0.10^{+0.01}_{-0.01} \times 10^{-1}$	$-1.93^{+0.05}_{-0.05}$	387^{+123}_{-116}	$0.75^{+0.10}_{-0.09} \times 10^{-6}$	$0.11^{+0.01}_{-0.02} \times 10^{-1}$	$-1.88^{+0.06}_{-0.07}$	$-5.01^{+2.57}_{-2.69}$	30^{+8}_{-9}	$0.75^{+0.28}_{-0.21} \times 10^{-6}$	0.4	1.5	1.5
33.075~47.327	35.24	$0.07^{+0.00}_{-0.00} \times 10^{-1}$	$-1.84^{+0.03}_{-0.03}$	493^{+81}_{-83}	$0.53^{+0.04}_{-0.04} \times 10^{-6}$	$0.07^{+0.01}_{-0.01} \times 10^{-1}$	$-1.87^{+0.08}_{-0.10}$	$-4.59^{+2.50}_{-2.80}$	74^{+20}_{-27}	$0.62^{+0.28}_{-0.19} \times 10^{-6}$	-11.8	2.2	-7.3
47.327~73.490	28.11	$0.05^{+0.01}_{-0.01} \times 10^{-1}$	$-1.83^{+0.06}_{-0.06}$	583^{+268}_{-250}	$0.35^{+0.06}_{-0.06} \times 10^{-6}$	$0.06^{+0.01}_{-0.01} \times 10^{-1}$	$-1.71^{+0.08}_{-0.07}$	$-4.03^{+1.90}_{-2.91}$	67^{+15}_{-14}	$0.34^{+0.12}_{-0.09} \times 10^{-6}$	-2.7	1.0	-0.7

Note. Column (1): the start and stop times (in units of s) of the BBlocks time bins. Column (2): the significance S . Columns (3–6): the best-fit parameters for the CPL model. Columns (7–11): the best-fit parameters for the Band model. Column (12): the difference between the DICs for the CPL and Band models; $\Delta\text{DIC} = \text{DIC}_{\text{Band}} - \text{DIC}_{\text{CPL}}$. Columns (13–14): the effective number of parameters (p_{DIC}) for the CPL and Band models, respectively.

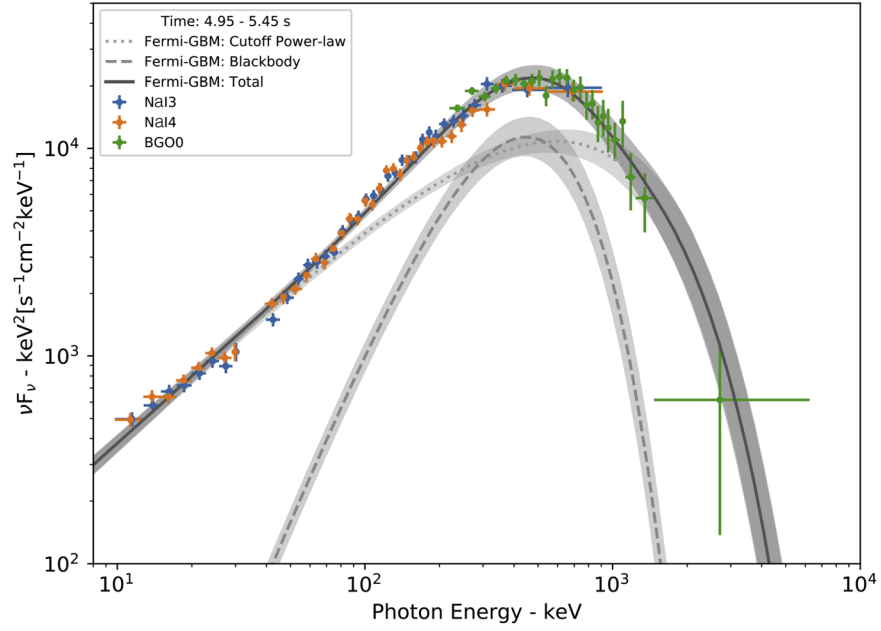


Figure 5. Spectrum from 4.95 to 5.45 s. The spectrum includes data from Fermi-GBM (2 Na I and 1 BGO detector). The fitting is presented by the solid line, including the components of a Planck BB function, indicated by the dashed line, and a CPL function, indicated by the dotted line.

Table 4
Spectral Parameters of the Slices Having a Thermal Component in GRB 190114C

	$t_{\text{start}} \sim t_{\text{stop}}$ (s)	S	Model	ΔDIC DIC _(CPL+BB) –(CPL)	Temperature (keV)	Thermal Flux (erg cm ⁻² s ⁻¹)	Total Flux (erg cm ⁻² s ⁻¹)	Ratio
P_1^{th}	0.55~0.70	96.49	CPL+BB	-177	351^{+99}_{-100}	$0.59^{+1.82}_{-0.45} \times 10^{-5}$	$0.57^{+0.19}_{-0.11} \times 10^{-4}$	$0.10^{+0.32}_{-0.08}$
	0.70~0.98	153.65	CPL+BB	-285	283^{+59}_{-55}	$0.58^{+1.27}_{-0.42} \times 10^{-5}$	$0.72^{+0.15}_{-0.11} \times 10^{-4}$	$0.08^{+0.18}_{-0.06}$
	0.98~1.45	196.39	CPL+BB	-43	186^{+40}_{-34}	$0.91^{+1.72}_{-0.80} \times 10^{-5}$	$0.86^{+0.22}_{-0.24} \times 10^{-4}$	$0.10^{+0.20}_{-0.10}$
	1.45~1.58	105.17	CPL+BB	-148	163^{+20}_{-19}	$2.42^{+2.10}_{-1.13} \times 10^{-5}$	$1.05^{+0.03}_{-0.20} \times 10^{-4}$	$0.23^{+0.20}_{-0.11}$
	1.58~1.64	80.78	CPL+BB	-29	151^{+11}_{-11}	$5.26^{+2.68}_{-1.69} \times 10^{-5}$	$1.38^{+0.33}_{-0.28} \times 10^{-4}$	$0.36^{+0.21}_{-0.14}$
	1.64~1.71	83.47	CPL+BB	-21	136^{+28}_{-24}	$2.06^{+4.18}_{-1.63} \times 10^{-5}$	$1.49^{+0.68}_{-0.41} \times 10^{-4}$	$0.14^{+0.29}_{-0.12}$
	1.71~1.80	88.47	CPL+BB	-114	73^{+13}_{-18}	$0.09^{+0.20}_{-0.07} \times 10^{-5}$	$0.71^{+0.17}_{-0.41} \times 10^{-4}$	$0.01^{+0.03}_{-0.01}$
	1.80~1.93	80.82	CPL+BB	-139	30^{+4}_{-5}	$0.07^{+0.05}_{-0.04} \times 10^{-5}$	$0.32^{+0.02}_{-0.02} \times 10^{-4}$	$0.02^{+0.02}_{-0.01}$
P_2^{th}	2.45~2.64	152.16	CPL+BB	-21	174^{+13}_{-13}	$3.88^{+1.89}_{-1.40} \times 10^{-5}$	$1.76^{+0.26}_{-0.24} \times 10^{-4}$	$0.22^{+0.11}_{-0.09}$
	2.64~2.88	136.19	CPL+BB	-622	197^{+17}_{-16}	$4.07^{+1.91}_{-1.34} \times 10^{-5}$	$1.17^{+0.28}_{-0.28} \times 10^{-4}$	$0.35^{+0.18}_{-0.14}$
	2.88~3.09	103.16	CPL+BB	-12	188^{+22}_{-22}	$2.36^{+1.83}_{-1.11} \times 10^{-5}$	$1.01^{+0.38}_{-0.29} \times 10^{-4}$	$0.23^{+0.20}_{-0.13}$
	3.09~3.21	92.86	CPL+BB	-20	162^{+12}_{-8}	$4.93^{+1.71}_{-1.58} \times 10^{-5}$	$1.95^{+0.85}_{-0.57} \times 10^{-4}$	$0.25^{+0.14}_{-0.11}$
	3.21~3.60	146.18	CPL+BB	-37	149^{+7}_{-8}	$3.16^{+1.03}_{-0.79} \times 10^{-5}$	$1.36^{+0.47}_{-0.31} \times 10^{-4}$	$0.23^{+0.11}_{-0.08}$
	3.60~3.74	82.69	CPL+BB	-20	151^{+11}_{-11}	$3.36^{+1.65}_{-1.28} \times 10^{-5}$	$1.23^{+0.84}_{-0.49} \times 10^{-4}$	$0.27^{+0.23}_{-0.15}$
	3.74~3.96	140.29	CPL+BB	-63	140^{+5}_{-5}	$7.11^{+1.13}_{-1.01} \times 10^{-5}$	$2.23^{+0.81}_{-0.55} \times 10^{-4}$	$0.32^{+0.13}_{-0.09}$
	3.96~4.10	130.66	CPL+BB	-44	108^{+6}_{-7}	$3.52^{+1.85}_{-1.83} \times 10^{-5}$	$1.79^{+1.71}_{-0.79} \times 10^{-4}$	$0.20^{+0.22}_{-0.13}$
	4.10~4.44	170.04	CPL+BB	-922	115^{+7}_{-7}	$1.89^{+0.80}_{-0.59} \times 10^{-5}$	$0.94^{+0.13}_{-0.11} \times 10^{-4}$	$0.20^{+0.09}_{-0.07}$
	4.44~4.51	69.23	CPL+BB	-207	97^{+15}_{-13}	$1.22^{+1.57}_{-0.74} \times 10^{-5}$	$0.55^{+0.23}_{-0.13} \times 10^{-4}$	$0.22^{+0.30}_{-0.15}$
	4.51~4.77	142.52	CPL+BB	-133	111^{+5}_{-5}	$3.45^{+1.02}_{-0.72} \times 10^{-5}$	$0.85^{+0.22}_{-0.16} \times 10^{-4}$	$0.41^{+0.16}_{-0.12}$
	4.77~4.95	134.52	CPL+BB	-54	90^{+4}_{-4}	$3.21^{+0.89}_{-0.76} \times 10^{-5}$	$0.97^{+0.33}_{-0.23} \times 10^{-4}$	$0.33^{+0.15}_{-0.11}$
	4.95~5.45	184.46	CPL+BB	-176	91^{+3}_{-3}	$2.45^{+0.45}_{-0.39} \times 10^{-5}$	$0.70^{+0.14}_{-0.10} \times 10^{-4}$	$0.35^{+0.09}_{-0.07}$
5.45~5.51	76.02	CPL+BB	-93	82^{+5}_{-5}	$3.18^{+1.30}_{-1.22} \times 10^{-5}$	$0.80^{+0.95}_{-0.32} \times 10^{-4}$	$0.40^{+0.49}_{-0.22}$	
5.51~5.65	100.84	CPL+BB	-27	53^{+4}_{-4}	$1.10^{+0.51}_{-0.43} \times 10^{-5}$	$0.44^{+0.11}_{-0.16} \times 10^{-4}$	$0.25^{+0.13}_{-0.12}$	
5.65~5.69	48.93	CPL+BB	-26	32^{+2}_{-2}	$1.07^{+0.33}_{-0.26} \times 10^{-5}$	$0.35^{+0.07}_{-0.06} \times 10^{-4}$	$0.30^{+0.11}_{-0.09}$	
T_{90}	0.00~116.00	190.61	CPL+BB	-266	132^{+4}_{-4}	$0.12^{+0.04}_{-0.03} \times 10^{-5}$	$0.06^{+0.01}_{-0.01} \times 10^{-4}$	$0.21^{+0.07}_{-0.05}$

Note. The spectra are best fitted by a two-component scenario, with a thermal BB component accompanied by a nonthermal CPL component. The columns show: the start and stop times of the BBBlocks slices; the significance; the best-fitting model; the ΔDIC between the CPL+BB and CPL models; the temperature; the thermal flux; the total flux; and the ratio of the thermal flux. The flux is defined in the energy band of 1 keV to 10 MeV. For the slices of ~ 3 s to ~ 4 s, the Band+BB model offers a goodness of fitting that is very close to that of the CPL+BB model, in terms of the global consistency, and considering that the time-integrated spectrum is best fitted by the CPL+BB model. Here, we perform all the thermal analysis using CPL+BB.

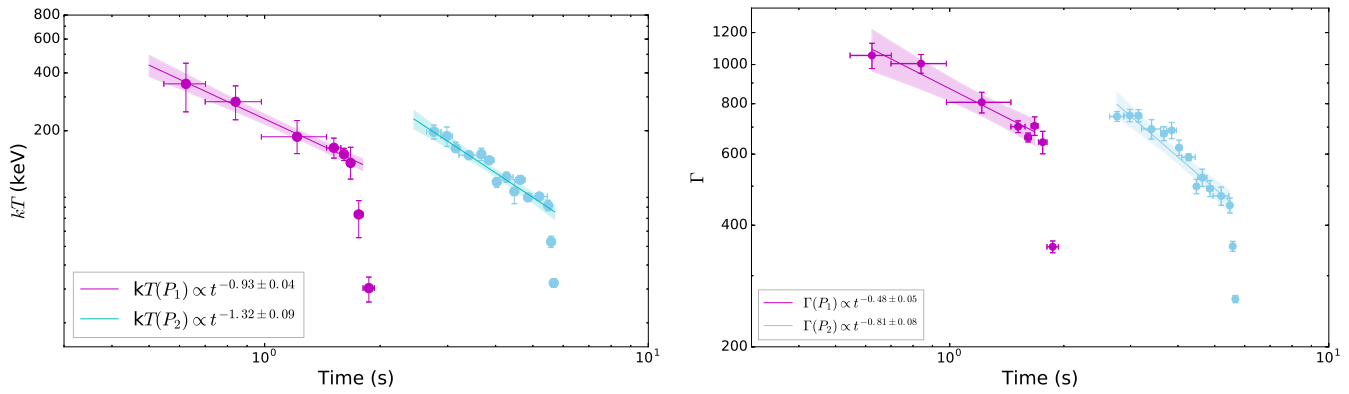


Figure 6. Temporal evolutions of the temperature kT (left) and bulk Lorentz factor Γ (right). The data points indicated by the pink and cyan colors represent the two different pulses. The solid lines show the best power-law fits to the data for P_1 and P_2 , excluding several points during the drop, and the shaded areas are their 2σ (95% confidence interval) regions. The derived time-resolved evolution of Γ is based on the photosphere properties under the framework of the traditional method (Pe’er et al. 2007).

5.3. Photosphere Properties

We compare the properties of the thermal components identified in P_1 and P_2 . The evolutions of the characteristic temperatures (kT) in P_1 and P_2 follow distinctly broken power-law decays: a smooth decay of the temperature is followed by a fast drop (see the left panel of Figure 6). The temporal features in each pulse are consistent with the typical observations, which show a temperature evolution with a broken power law in time (Ryde 2004; Ryde & Pe’er 2009), but such features in two independent pulses within one burst have never been identified in previous observations. The temporal behaviors showing different decay indices between two different pulses within a single GRB suggest that the GRB central engine ejects distinct independent jet components during its active phase. We note that several GRBs with statistically significant thermal components have previously been observed by BATSE, Konus, Swift, and Fermi (Ryde et al. 2010; Guiriec et al. 2011, 2013; Axelsson et al. 2012). However, these have either been single-pulse bursts (e.g., GRB 110721A; Axelsson et al. 2012) or highly overlapping multi-pulse bursts (e.g., GRB 090902B; Ryde et al. 2010), or their thermal emission component has not been strong enough (e.g., GRB 100724B; Guiriec et al. 2011), so that the photosphere properties could not be studied in detail among distinct pulses. The unique advantages of GRB 190114C—i.e., its low redshift, its high fluence, several well-separated pulses in one single GRB, and its strong thermal component—make such a study possible.

Within the framework of the standard fireball photosphere model (Pe’er et al. 2007), we can infer the photosphere characteristics and the ratio of thermal to nonthermal emission in order to obtain information about the jet properties, such as the bulk Lorentz factor Γ and the initial size of the jet r_0 . Figures 6 and 7 show the evolutions of the bulk Lorentz factor Γ and the parameter \mathfrak{R} , respectively, where \mathfrak{R} is the effective transverse size of the emitting region (Ryde & Pe’er 2009). They exhibit similar temporal behaviors in P_1 and P_2 , i.e., a broken power-law evolution behavior, with \mathfrak{R} increasing with time and Γ decreasing over time. The comparison of the properties from a global view, as well as the best-fitting results for the relevant parameters, are summarized in Table 5.

The derived Lorentz factors and photosphere radii exhibit systematic variations, with the Lorentz factor decreasing from ~ 1000 to ~ 200 (Figure 6) and the photosphere radius varying on the order of 10^{12} cm (Figure 7(a)). This is likely related to

the behavior of the GRB central engine. The decay of Γ in P_1 and P_2 is consistent with the expectation that faster ejecta from the engine tend to reach the photosphere earlier than slower ejecta, while the rapid decline at the end of each episode may be related to the abrupt cessation of the engine activity (Li & Zhang 2021), with the decay slope being defined by the ebbing ejection rate of the central engine. Since the Lorentz factor range is not very wide, it is expected that the deceleration of the fireball will be essentially prompt, without a significant energy injection phase due to the pileup of the slow materials. This is consistent with a power-law decay with the time of the multiwavelength afterglow emission from the source (MAGIC Collaboration et al. 2019b; Wang et al. 2019b, 2019a).

5.4. Application to GRB 190114C with Our New Method

In short, GRB 190114C is unique in terms of the following aspects. (1) It has three well-separated emission episodes, which can be defined as the first, second, and third pulses. (2) The emissions of the first two main pulses consist of two strong thermally subdominated episodes, which independently exhibit similar temporal properties. (3) The first two pulses (thermal) and the third pulse (nonthermal) have distinct spectral properties. (4) The thermal component has a thermal-to-total flux ratio of $21_{-4}^{+6}\%$, which is the second highest among the GRBs observed with Fermi-GBM so far (the highest one being observed in GRB 090902B, with a thermal flux ratio $\sim 70\%$). (5) Strong TeV emission was observed, setting the record for one of the highest photon energy in any GRB (MAGIC Collaboration et al. 2019b). The two well-separated pulses with independent and analogous thermal component evolution patterns make this extraordinarily bright GRB a unique event for studying the jet composition and the evolution of the photospheric properties in a single GRB. We note that several interesting cases have been observed in the past. For example, in some GRBs, a hot fireball jet characterized by a quasi-thermal Planck-like spectrum has been observed (e.g., GRB 090902B; Abdo et al. 2009). In many other GRBs, a Poynting flux-dominated outflow characterized by a Band (or CPL)-only function may also be observed (e.g., GRB 080916C; Abdo et al. 2009; and GRB 130427A; Preece et al. 2016). More interestingly, we may also observe a hybrid jet characterized by either a two-component spectral scenario (composed of a nonthermal component and a thermal component simultaneously, e.g., GRB 110721A;

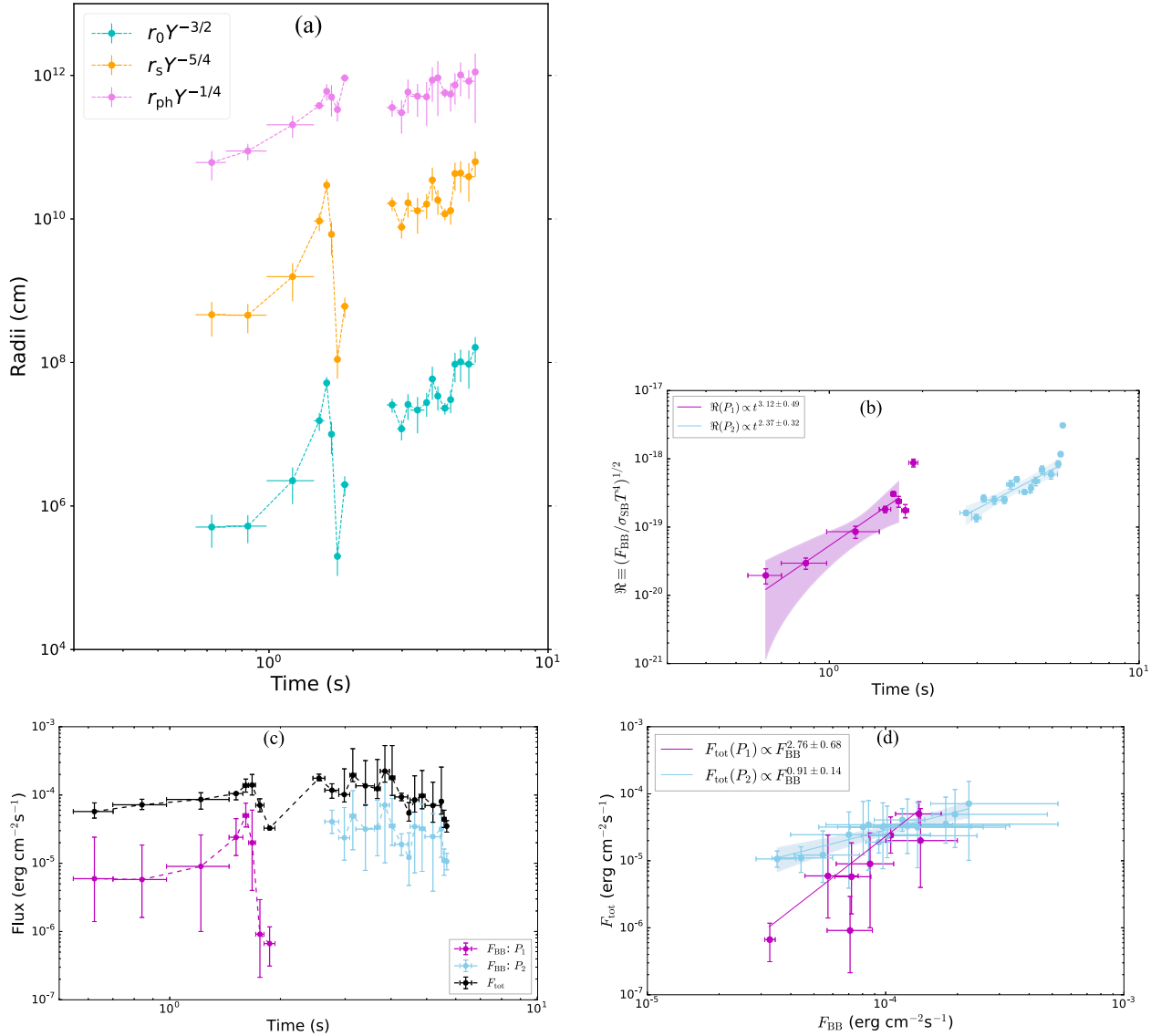


Figure 7. Pulse-wise properties of GRB 190114C. (a) Temporal evolutions of the photospheric radius r_{ph} (violet), the saturation radius r_s (orange), and the nozzle radius r_0 (cyan). (b) Temporal evolution of the parameter \mathfrak{R} . (c) Temporal evolutions of the blackbody energy flux (F_{BB}) and the total energy flux (F_{tot}). (d) The total energy flux (F_{tot}) vs. the blackbody energy flux (F_{BB}). The color notations are the same as in Figure 6.

Axelsson et al. 2012; Gao & Zhang 2015; or a transition from a fireball to a Poynting flux-dominated outflow within a single GRB, e.g., GRB 160625B; Ryde et al. 2011; Zhang et al. 2018; Li 2019a). However, GRB 190114C presents unique information that has not been available before.

The two abovementioned methods (see Section 5.3) for measuring Lorentz factors both rely on some unknown parameters. By combining the photosphere data in P_1 and P_2 and the afterglow data in P_{AO} , one can discriminate the various energy components in the fireball in an essentially parameter-independent way (Zhang et al. 2021). A systematic search of the previously detected GRBs did not reveal a single case showing both a significant photosphere signature and an afterglow deceleration signature (Zhang et al. 2021). GRB 190114C, therefore, provides the first case in which the determination of the fireball parameters (Zhang et al. 2021) can be carried out. We perform a time-integrated spectral fit to the prompt emission spectra of P_1 and P_2 (0.55–1.93 s and 2.45–5.69 s, respectively) with the CPL+BB model and derive the observed properties (including both the thermal and

nonthermal components) of the fireball, as shown in Table 6. Following Zhang et al. (2021; for details, see Section 4.2), we can derive the following physical parameters of a GRB fireball (Table 6): the initial dimensionless specific enthalpy $\eta = 854 \pm 38$; the bulk Lorentz factor at the photosphere $\Gamma_{\text{ph}} = 833 \pm 38$; the bulk Lorentz factor before deceleration $\Gamma_0 = 719 \pm 59$; and the fireball isotropic equivalent mass loading $M_{\text{iso}} = (1.7 \pm 0.4) \times 10^{-3} M_{\odot}$. This gives a direct measurement of the fireball radiative efficiency $\eta_{\gamma} = (15.8 \pm 5.4)\%$. This measured efficiency has much smaller uncertainties than the values derived for previous GRBs using afterglow modeling (Zhang et al. 2007). A high fireball radiative efficiency has been theorized in the past (Mészáros & Rees 2000; Kobayashi & Sari 2001). Our measured $\eta_{\gamma} \sim 16\%$ suggests that a GRB fireball can indeed emit both thermal and nonthermal gamma-rays efficiently. We also find that the derived bulk Lorentz factors measured during the prompt emission phase ($\Gamma = 854 \pm 38$) are slightly higher than the bulk Lorentz factor measured at the deceleration radius ($\Gamma_0 = 719 \pm 59$). This is fully consistent with the picture

Table 5
Thermal-pulse Properties of GRB 190114C

	P_1^{th} (From $t_{\text{obs}} = 0.55$ to 1.93 s)	P_2^{th} (From $t_{\text{obs}} = 2.45$ to 5.69 s)
Observed Properties		
Duration	1.38 s	3.24 s
Spectral cutoff energy [E_c]	337_{-27}^{+27} (keV)	605_{-17}^{+17} (keV)
Temperature [kT]	267_{-18}^{+22} (keV)	145_{-3}^{+3} (keV)
Thermal energy flux [F_{BB}]	$(1.51_{-0.68}^{+0.97}) \times 10^{-5}$ (erg cm $^{-2}$ s $^{-1}$)	$(2.32_{-0.30}^{+0.35}) \times 10^{-5}$ (erg cm $^{-2}$ s $^{-1}$)
Total energy flux [F_{tot}]	$(8.65_{-1.34}^{+1.64}) \times 10^{-5}$ (erg cm $^{-2}$ s $^{-1}$)	$(1.07_{-0.05}^{+0.05}) \times 10^{-4}$ (erg cm $^{-2}$ s $^{-1}$)
Flux ratio [$F_{\text{BB}}/F_{\text{tot}}$]	$0.17_{-0.08}^{+0.12}$	$0.22_{-0.03}^{+0.03}$
Thermal fluence [S_{BB}]	$(2.09_{-0.94}^{+1.35}) \times 10^{-5}$ (erg cm $^{-2}$)	$(7.51_{-0.97}^{+1.13}) \times 10^{-5}$ (erg cm $^{-2}$)
Total fluence [S_{tot}]	$(1.20_{-0.19}^{+0.23}) \times 10^{-4}$ (erg cm $^{-2}$)	$(3.46_{-0.17}^{+0.17}) \times 10^{-4}$ (erg cm $^{-2}$)
Isotropic thermal luminosity [$L_{\text{BB},\gamma,\text{iso}}$]	$(1.04_{-0.47}^{+0.67}) \times 10^{52}$ (erg s $^{-1}$)	$(1.60_{-0.21}^{+0.24}) \times 10^{52}$ (erg s $^{-1}$)
Isotropic total luminosity [$L_{\gamma,\text{iso}}$]	$(5.95_{-0.92}^{+1.13}) \times 10^{52}$ (erg s $^{-1}$)	$(7.36_{-0.34}^{+0.34}) \times 10^{52}$ (erg s $^{-1}$)
Isotropic thermal energy [$E_{\text{BB},\gamma,\text{iso}}$]	$(1.01_{-0.46}^{+0.65}) \times 10^{52}$ (erg)	$(3.64_{-0.47}^{+0.55}) \times 10^{52}$ (erg)
Isotropic total energy [$E_{\gamma,\text{iso}}$]	$(5.81_{-0.91}^{+1.10}) \times 10^{52}$ (erg)	$(1.68_{-0.08}^{+0.08}) \times 10^{53}$ (erg)
Photospheric Properties		
Nozzle radius [r_0]	$(8.55 \pm 2.8) \times 10^6$ (cm)	$(5.00 \pm 0.48) \times 10^7$ (cm)
Saturation radius [r_s]	$(4.31 \pm 1.53) \times 10^9$ (cm)	$(1.96 \pm 0.19) \times 10^{10}$ (cm)
Photospheric radius [r_{ph}]	$(5.33 \pm 0.47) \times 10^{11}$ (cm)	$(1.41 \pm 0.04) \times 10^{12}$ (cm)
Parameter Evolution		
Temperature [$kT(t)$]	$\propto t^{-0.93 \pm 0.04}$	$\propto t^{-1.32 \pm 0.09}$
Effective transverse size [$\mathfrak{R}(t)$]	$\propto t^{3.12 \pm 0.49}$	$\propto t^{2.37 \pm 0.32}$
Bulk Lorentz factor [$\Gamma(t)$]	$\propto t^{-0.48 \pm 0.05}$	$\propto t^{-0.81 \pm 0.08}$
Nozzle radius R_0 (cm)	$\propto t^{4.69 \pm 3.89}$	$\propto t^{4.10 \pm 0.86}$
Saturation radius R_s (cm)	$\propto t^{4.47 \pm 4.20}$	$\propto t^{2.10 \pm 0.96}$
photospheric radius R_{ph} (cm)	$\propto t^{1.76 \pm 0.60}$	$\propto t^{1.09 \pm 0.37}$

Table 6
Global Properties of GRB 190114C

Measured Parameters	
Isotropic equivalent thermal energy [$E_{\text{th,iso}}$]	$(3.69_{-0.67}^{+0.78}) \times 10^{52}$ erg
Isotropic equivalent nonthermal energy [$E_{\text{nth,iso}}$]	$[(1.92_{-0.11}^{+0.12}) \times 10^{53}(\text{GBM}) + 8.49_{-1.80}^{+1.80} \times 10^{51}(\text{LAT})]$ erg
Thermal energy flux [$F_{\text{BB}}^{\text{obs}}$]	$(1.27_{-0.23}^{+0.27}) \times 10^{-5}$ erg cm $^{-2}$ s $^{-1}$
Total energy flux [F_{γ}^{obs}]	$[(7.91_{-0.32}^{+0.33}) \times 10^{-5}(\text{GBM}) + 3.41_{-0.69}^{+0.69} \times 10^{-6}(\text{LAT})]$ erg cm $^{-2}$ s $^{-1}$
Deceleration time [t_{dec}]	6–10 s
Temperature [kT^{obs}]	163 ± 6 keV
Redshift [z]	0.4254 ± 0.0005
Derived Parameters	
Dimensionless specific enthalpy [η]	854 ± 38
Bulk Lorentz factor at r_{ph} [Γ_{ph}]	833 ± 38
Initial Lorentz factor [Γ_s]	719 ± 59
Isotropic equivalent total mass [M_{iso}]	$(1.7 \pm 0.4) \times 10^{-3} M_{\odot}$
Isotropic kinetic energy [$E_{\text{k,iso}}$]	$(1.6 \pm 0.7) \times 10^{54}$ erg
Isotropic total energy [$E_{\text{tot,iso}}$]	$(1.8 \pm 0.7) \times 10^{54}$ erg
Gamma-ray radiative efficiency [η_{γ}]	$15.8 \pm 5.4\%$
Further Derived Parameters	
Energy fractions assigned to electric fields [$\epsilon_{e,-1}$]	1.11 ± 0.01
Energy fractions assigned to magnetic fields [$\epsilon_{B,-2}$]	0.05 ± 0.01
Characteristic synchrotron frequency [ν_{m}]	$(1.30 \pm 0.82) \times 10^{17}$ Hz
Cooling frequency [ν_{c}]	$(4.44 \pm 0.66) \times 10^{17}$ Hz
Klein–Nishina frequency [ν_{KN}]	$(6.55 \pm 0.16) \times 10^{17}$ Hz

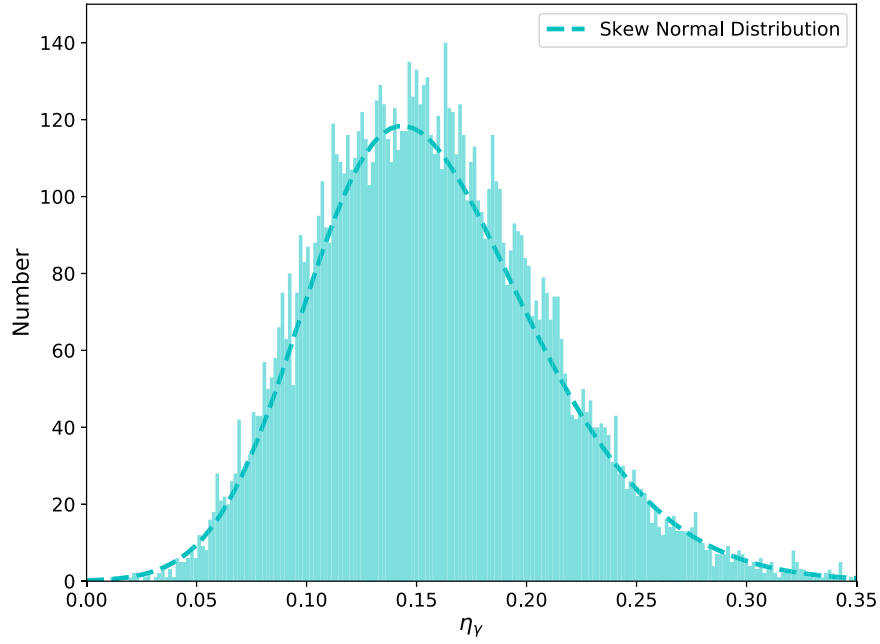


Figure 8. Histogram of η_γ from 10,000 MC samplings; each bin corresponds to the η_γ interval of 0.003. The histogram is fitted by a skew-normal distribution function.

described by the GRB fireball model, in which a fraction of the kinetic energy is dissipated during the prompt emission phase.

To solve the above equations described in Section 4.2, we apply the MC method to obtain the mean and uncertainty for the measured values and uncertainties of $E_{\text{th,iso}}$, $E_{\text{nth,iso}}$, $F_{\text{BB}}^{\text{obs}}$, F_γ^{obs} , kT^{obs} . For each of them, we sample 10,000 times, following the normal distribution. We set a range of 6–10 s for t_{dec} , while we use 0.5–1.5 cm^{-3} for n . We obtain the values of η , Γ_{ph} , Γ_0 , M_{iso} , $E_{\text{k,iso}}$, $E_{\text{tot,iso}}$, and η_γ , computed from the 10,000 samples using the above equations, and find that they can be fitted by skew-normal distributions, see, e.g., Figure 8, from which the mean and asymmetrical uncertainties are derived. The average values based on the two thermal episodes of P_1^{th} (from 0.55 to 1.93 s) and P_2^{th} (from 2.45 to 5.69 s) are given in Table 6. All the measured quantities are presented in the upper panel, with all the derived parameters being presented in the lower panel.

5.5. Further Estimate of the Energy Fractions Assigned to Electrons (ϵ_e) and Magnetic (ϵ_B) Fields

Once E_k has been precisely obtained from the observational data, using our new methods discussed above, one can estimate the energy fractions assigned to the electrons (ϵ_e) and magnetic fields (ϵ_B) using the afterglow models (Zhang et al. 2007).

The isotropic blastwave kinetic energy ($E_{\text{k,iso}}$) can also be measured from the afterglow emission (normal decay) using the Swift-XRT data. For a constant-density ISM, e.g., Schulze et al. (2011), the characteristic synchrotron frequency and the cooling frequency of the minimum-energy-injected electrons, and therefore the peak spectral flux, can be given by Sari et al. (1998), Yost et al. (2003), Zhang et al. (2007):

$$\nu_m = 3.3 \times 10^{12} \text{Hz} \left(\frac{p-2}{p-1} \right)^2 \times (1+z)^{1/2} \epsilon_{\text{B},-2}^{1/2} \epsilon_{\text{e},-1}^2 E_{\text{K,iso},52}^{1/2} t_d^{-3/2}, \quad (15)$$

$$\nu_c = 6.3 \times 10^{15} \text{Hz} (1+z)^{-1/2} (1+Y)^{-2} \times \epsilon_{\text{B},-2}^{-3/2} E_{\text{K,iso},52}^{-1/2} n^{-1} t_d^{-1/2}, \quad (16)$$

$$F_{\nu,\text{max}} = 1.6 \text{mJy} (1+z) D_{28}^{-2} \epsilon_{\text{B},-2}^{1/2} E_{\text{K,iso},52} n^{-1}, \quad (17)$$

where p is the electron spectral distribution index, ϵ_e and ϵ_B are the energy fractions assigned to the electrons and the magnetic fields, t_d is the time in the observer frame in units of days, $D_{28} = D/10^{28}$ is the luminosity distance in units¹⁹ of 10^{28} cm, n is the number density in the constant-density ambient medium, and

$$Y = [-1 + (1 + 4\eta_1\eta_2\epsilon_e/\epsilon_B)^{1/2}]/2 \quad (18)$$

is the Inverse Compton (IC) parameter, where $\eta_1 = \min[1, (\nu_c/\nu_m)^{(2-p)/2}]$, $\eta_2 = \min[1, (\nu_{\text{KN}}/\nu_c)^{(3-p)/2}]$ (for the slow-cooling $\nu_m < \nu_x < \nu_c$ case) is a correction factor introduced by the Klein–Nishina effect, where ν_{KN} is the Klein–Nishina frequency:

$$\nu_{\text{KN}} = h^{-1} \Gamma m_e c^2 \gamma_{e,X}^{-1} (1+z)^{-1} \simeq 2.4 \times 10^{15} \text{Hz} (1+z)^{-3/4} E_{\text{K,iso},52}^{1/4} \epsilon_{\text{B},-2}^{1/4} t_d^{-3/4} \nu_{18}^{-1/2}, \quad (19)$$

where h is Planck’s constant and $\gamma_{e,X}$ is the electron Lorentz factor corresponding to the X-ray band emission.

The spectral regime can be determined using the closure relation in the afterglow emission via the observed temporal ($\hat{\alpha}$) and spectral ($\hat{\beta}$) indices. The temporal index $\hat{\alpha}_{\text{XRT}}$ is measured from the Swift-XRT light curve (see Figure 3 (a)) and the corresponding spectral index $\hat{\beta}_{\text{XRT}} = -(\Gamma_{\text{XRT}} - 1) = -0.93 \pm 0.10$ (Γ_{XRT} is the photon spectral index) is available from the Swift online server (Evans et al. 2007, 2009).²⁰ Using the temporal and spectral indices, one

¹⁹ The convention $Q = 10^x Q_x$ is adopted in cgs units for all parameters throughout the paper.

²⁰ https://www.swift.ac.uk/burst_analyser/

can therefore determine that the X-ray emission in GRB 190114C is in the $\nu_m < \nu_x < \nu_c$ regime. With the spectral regime known, the electron index p can be derived using the observed temporal index: $p = (3 - 4\hat{\alpha}_{\text{XRT}})/3 = 2.85 \pm 0.01$.

In the case of $p > 2$, in the $\nu_m < \nu_x < \nu_c$ regime, one can derive the X-ray band energy flux as

$$\begin{aligned} \nu F_\nu(\nu = 10^{18}\text{Hz}) &= F_{\nu,\text{max}}(\nu_m/\nu_x)^{(p-1)/2} \\ &= 6.5 \times 10^{-13} \text{erg s}^{-1} \text{cm}^{-2} D_{28}^{-2} (1+z)^{(p+3)/4} \\ &\times f_p \epsilon_{B,-2}^{(p+1)/4} \epsilon_{e,-1}^{p-1} E_{\text{K,iso},52}^{(p+3)/4} n^{1/2} t_d^{(3-3p)/4} \nu_{18}^{(3-p)/2}. \end{aligned} \quad (20)$$

This gives

$$\begin{aligned} E_{\text{K,iso},52} &= \left[\frac{\nu F_\nu(\nu = 10^{18}\text{Hz})}{6.5 \times 10^{-13} \text{erg s}^{-1} \text{cm}^{-2}} \right]^{4/(p+3)} \\ &\times D_{28}^{8/(p+3)} (1+z)^{-1} t_d^{3(p-1)/(p+3)} \\ &\times f_p^{-4/(p+3)} \epsilon_{B,-2}^{-(p+1)/(p+3)} \epsilon_{e,-1}^{4(1-p)/(p+3)} \\ &\times n^{-2/(p+3)} \nu_{18}^{2(p-3)/(p+3)}, \end{aligned} \quad (21)$$

where $\nu F_\nu(\nu = 10^{18})$ Hz is the energy flux at the frequency 10^{18} Hz in units of $\text{erg s}^{-1} \text{cm}^{-2}$ and

$$f_p = 6.73 \left(\frac{p-2}{p-1} \right)^{p-1} (3.3 \times 10^{-6})^{(p-2.3)/2} \quad (22)$$

is a function of the electron power-law index p .

Simultaneously solving Equations (18) and (21) with the IC parameter $Y^{\text{IC}} (= E_{\text{GeV}}/E_{\text{MeV}})$ constrained from the observations of GRB 190114C, e.g., $Y^{\text{IC}} = 0.75$ (e.g., Wang et al. 2019a), and using the episodes of P_1^{th} and P_2^{th} , we obtain ϵ_B and ϵ_e during the time interval of P_{AO} :

$$\begin{cases} \epsilon_{e,-1} = 1.11 \pm 0.01, \\ \epsilon_{B,-2} = 0.05 \pm 0.01 \end{cases} \quad (23)$$

Knowing the values of ϵ_B and ϵ_e , we can also solve for ν_m , ν_c , and ν_{KN} :

$$\begin{cases} \nu_m = (1.30 \pm 0.82) \times 10^{17} \text{Hz}, \\ \nu_c = (4.44 \pm 0.66) \times 10^{17} \text{Hz}, \\ \nu_{\text{KN}} = (6.55 \pm 0.16) \times 10^{17} \text{Hz} \end{cases} \quad (24)$$

6. Conclusions

In this paper, using the photosphere data observed in P_1 and P_2 , and the early afterglow data observed in P_{AO} , as well as a measured redshift, we apply the method proposed in Zhang et al. (2021) to directly dissect the GRB fireball energy budget and therefore to measure the GRB radiative efficiency for GRB 190114C.




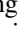
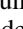
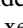




We first performed a detailed time-integrated and time-resolved spectral analysis of the Fermi-GBM observations, using various GRB spectral models. The prompt emission consists of three well-separated pulses. We found that strong thermal components were observed in the first two emission pulses. The spectra in P_1 and P_2 are best fitted by a two-component scenario, with a nonthermal Band-like component accompanied by a thermal BB component. The thermal component has a thermal-to-total flux ratio of $21_{-4}^{+6}\%$. Such a strong thermal component being found in the time-resolved spectral analysis of the well-separated pulses in GRB 190114C

provides a good opportunity to study the photospheric properties, allowing us for the first time to conduct a fine time-resolved spectral analysis and track the blackbody evolution among the different pulses in a single GRB. Indeed, we found two well-separated thermal pulses, evolving independently and analogically, inferred from their observational and physical parameters as derived from the fireball model. Such independent and analogical pulse-wise thermal properties in GRB 190114C comprise the first such case to be found in GRB history, strongly supporting the evidence for there being a shell-like structure during the prompt emission phase. We also found that starting from the third pulse (P_3), and extending to the entire afterglow, the spectra are all nonthermal and the synchrotron plus Compton upscattering model well interprets the observations, so consequently the fireball parameters are obtained. More interestingly, the onset signature of afterglow emission corresponding to the deceleration of the fireball was observed to occur from T_0+6 s to T_0+15 s in P_{AO} , due to the fact that multiple pieces of observational evidence (e.g., the flux, energy band, and power-law index) are consistent with the external shock emissions. By incorporating the thermal (P_1 and P_2) and the nonthermal (P_{AO}) observations, as well as the photosphere and synchrotron radiative mechanisms, we directly derived the fireball energy budget, with little dependence on hypothetical parameters (Zhang et al. 2021), and measured a 16% radiative efficiency for this GRB.

With the fireball parameters that have been determined, the isotropic kinetic energy (Panaitescu & Kumar 2001) of the fireball at the afterglow phase is measured as $E_{\text{k,iso}} = (1.6 \pm 0.7) \times 10^{54}$ erg. This allows us to make use of this prompt emission-measured $E_{\text{k,iso}}$ in the afterglow model to constrain the shock microphysics parameters. Using broadband afterglow data, we can derive an electron injection power-law index $p \simeq 2.85$ and an IC parameter $Y^{\text{IC}} \sim 0.75$. This leads to the determination of the two equipartition parameters of the electrons and magnetic fields: $\epsilon_e = (1.11 \pm 0.01) \times 10^{-1}$ and $\epsilon_B = (0.5 \pm 0.1) \times 10^{-3}$, respectively. These parameters are usually poorly constrained in other GRBs, unless there is complete multiwavelength afterglow data (Panaitescu & Kumar 2002). We are able to measure these values more precisely, and they are also broadly consistent with the afterglow modeling of the event (MAGIC Collaboration et al. 2019b).

We thank the anonymous referee for the valuable comments and suggestions. We also thank Damien Bégué, Hüsne Dereli-Bégué, Michael S. Briggs, Xue-Feng Wu, Zi-Gao Dai, Ye-Fei Yuan, Yi-Fu Cai, En-Wei Liang, Remo Ruffini, and ICRANet members for many helpful discussions on GRB physics and phenomena. In particular, L.L. would like to dedicate this piece to the memory of Dr. Magnus Axelsson, a close colleague who passed away recently and was one of its main contributors. A.J. C.-T. acknowledges financial support from the State Agency for Research of the Spanish MCIU, through the ‘‘Center of Excellence Severo Ochoa’’ award to the Instituto de Astrofísica de Andalucía (SEV-2017-0709). D.A.K. acknowledges support from Spanish National Research Project RTI2018-098104-J-I00 (GRBPhot). We also acknowledge the use of public data from the Fermi Science Support Center (FSSC) and the UK Swift Science Data Center.

ORCID iDs

Liang Li  <https://orcid.org/0000-0002-1343-3089>
 Felix Ryde  <https://orcid.org/0000-0002-9769-8016>
 Asaf Pe'er  <https://orcid.org/0000-0001-8667-0889>
 Bing Zhang  <https://orcid.org/0000-0002-9725-2524>
 Sylvain Guiriec  <https://orcid.org/0000-0001-5780-8770>
 D. Alexander Kann  <https://orcid.org/0000-0003-2902-3583>
 Magnus Axelsson  <https://orcid.org/0000-0003-4378-8785>
 Kim Page  <https://orcid.org/0000-0001-5624-2613>
 Péter Veres  <https://orcid.org/0000-0002-2149-9846>
 P. N. Bhat  <https://orcid.org/0000-0001-7916-2923>

References

- Abdo, A. A., Ackermann, M., Ajello, M., et al. 2009, *ApJL*, 706, L138
 Abdo, A. A., Ackermann, M., Arimoto, M., et al. 2009, *Sci*, 323, 1688
 Acuner, Z., Ryde, F., Pe'er, A., Mortlock, D., & Ahlgren, B. 2020, *ApJ*, 893, 128
 Ajello, M., Arimoto, M., Axelsson, M., et al. 2020, *ApJ*, 890, 9
 Alexander, K. D., Laskar, T., Berger, E., Mundell, C. G., & Margutti, R. 2019, *GCN*, 23726, 1
 Axelsson, M., Baldini, L., Barbiellini, G., et al. 2012, *ApJL*, 757, L31
 Band, D., Matteson, J., Ford, L., et al. 1993, *ApJ*, 413, 281
 Battelino, M., Ryde, F., Omodei, N., & Band, D. L. 2007, in *AIP Conf. Ser.* 921, *The First GLAST Symposium*, ed. S. Ritz, P. Michelson, & C. A. Meegan (Melville, NY: AIP), 478
 Bégué, D., & Iyyani, S. 2014, *ApJ*, 792, 42
 Bikmaev, I., Irtuganov, E., Sakhibullin, N., et al. 2019, *GCN*, 23766, 1
 Bolmer, J., & Schady, P. 2019, *GCN*, 23702, 1
 Cash, W. 1979, *ApJ*, 228, 939
 Castro-Tirado, A. J., Hu, Y., Fernandez-Garcia, E., et al. 2019, *GCN*, 23708, 1
 Chevalier, R. A., & Li, Z.-Y. 1999, *ApJL*, 520, L29
 Dai, Z. G., & Lu, T. 1998, *MNRAS*, 298, 87
 de Ugarte Postigo, A., Thöne, C. C., Martín, S., et al. 2020, *A&A*, 633, A68
 Evans, P. A., Beardmore, A. P., Page, K. L., et al. 2007, *A&A*, 469, 379
 Evans, P. A., Beardmore, A. P., Page, K. L., et al. 2009, *MNRAS*, 397, 1177
 Foreman-Mackey, D., Hogg, D. W., Lang, D., & Goodman, J. 2013, *PASP*, 125, 306
 Gao, H., & Zhang, B. 2015, *ApJ*, 801, 103
 Ghirlanda, G., Bosnjak, Z., Ghisellini, G., Tavecchio, F., & Firmani, C. 2007, *MNRAS*, 379, 73
 Goldstein, A., Burgess, J. M., Preece, R. D., et al. 2012, *ApJ*, 199, 19
 Goodman, J. 1986, *ApJL*, 308, L47
 Guiriec, S., Connaughton, V., Briggs, M. S., et al. 2011, *ApJL*, 727, L33
 Guiriec, S., Daigne, F., Hascoët, R., et al. 2013, *ApJ*, 770, 32
 Hamburg, R., Veres, P., Meegan, C., et al. 2019, *GCN*, 23707, 1
 Im, M., Paek, G. S., Kim, S., Lim, G., & Choi, C. 2019a, *GCN*, 23717, 1
 Im, M., Paek, G. S. H., & Choi, C. 2019b, *GCN*, 23757, 1
 Gropp, J. D., Kennea, J. A., Krimm, N. J. K. P. H. A., et al. 2019, *GCN*, 23688, 1
 Jordana-Mitjans, N., Mundell, C. G., Kobayashi, S., et al. 2020, *ApJ*, 892, 97
 Kim, J., & Im, M. 2019, *GCN*, 23732, 1
 Kim, J., Im, M., Lee, C. U., et al. 2019, *GCN*, 23734, 1
 Kobayashi, S., & Sari, R. 2001, *ApJ*, 551, 934
 Kobayashi, S., & Zhang, B. 2003, *ApJ*, 597, 455
 Kocevski, D., Omodei, N., Axelsson, M., et al. 2019, *GCN*, 23709, 1
 Laskar, T., Alexander, K. D., Gill, R., et al. 2019, *ApJL*, 878, L26
 Li, L. 2019a, *ApJ*, 242, 16
 Li, L. 2019b, *ApJS*, 245, 7
 Li, L., & Zhang, B. 2021, *ApJS*, 253, 43
 Liang, E.-W., Li, L., Gao, H., et al. 2013, *ApJ*, 774, 13
 Liang, E.-W., Yi, S.-X., Zhang, J., et al. 2010, *ApJ*, 725, 2209
 Lloyd-Ronning, N. M., & Zhang, B. 2004, *ApJ*, 613, 477
 MAGIC Collaboration, Acciari, V. A., Ansoldi, S., et al. 2019a, *Natur*, 575, 459
 MAGIC Collaboration, Acciari, V. A., Ansoldi, S., et al. 2019b, *Natur*, 575, 455
 Mazaeva, E., Pozanenko, A., Volnova, A., Belkin, S., & Krugov, M. 2019, *GCN*, 23741, 1
 Melandri, A., Izzo, L., Pian, E., et al. 2022, *A&A*, 659, A39
 Meszaros, P., & Rees, M. J. 1993, *ApJL*, 418, L59
 Mészáros, P., & Rees, M. J. 2000, *ApJ*, 530, 292
 Mészáros, P., Rees, M. J., & Wijers, R. A. M. J. 1998, *ApJ*, 499, 301
 Misra, K., Resmi, L., Kann, D. A., et al. 2021, *MNRAS*, 504, 5685
 Narayana Bhat, P., Meegan, C. A., von Kienlin, A., et al. 2016, *ApJS*, 223, 28
 Paczynski, B. 1986, *ApJL*, 308, L43
 Panaitescu, A., & Kumar, P. 2001, *ApJL*, 560, L49
 Panaitescu, A., & Kumar, P. 2002, *ApJ*, 571, 779
 Pe'er, A. 2015, *AdAst*, 2015, 907321
 Pe'er, A., Ryde, F., Wijers, R. A. M. J., Mészáros, P., & Rees, M. J. 2007, *ApJL*, 664, L1
 Planck Collaboration, Aghanim, N., Akrami, Y., et al. 2020, *A&A*, 641, A6
 Preece, R., Goldstein, A., Bhat, N., et al. 2016, *ApJ*, 821, 12
 Preece, R. D., Briggs, M. S., Mallozzi, R. S., et al. 1998, *ApJL*, 506, L23
 Ravasio, M. E., Oganesyan, G., Salafia, O. S., et al. 2019, *A&A*, 626, A12
 Rees, M. J., & Meszaros, P. 1994, *ApJL*, 430, L93
 Ryde, F. 2004, *ApJ*, 614, 827
 Ryde, F. 2005, *ApJL*, 625, L95
 Ryde, F., & Pe'er, A. 2009, *ApJ*, 702, 1211
 Ryde, F., Axelsson, M., Zhang, B. B., et al. 2010, *ApJL*, 709, L172
 Ryde, F., Pe'er, A., Nymark, T., et al. 2011, *MNRAS*, 415, 3693
 Sari, R., & Piran, T. 1999, *ApJ*, 520, 641
 Sari, R., Piran, T., & Narayan, R. 1998, *ApJL*, 497, L17
 Scargle, J. D., Norris, J. P., Jackson, B., & Chiang, J. 2013, *ApJ*, 764, 167
 Schulze, S., Klose, S., Björnsson, G., et al. 2011, *A&A*, 526, A23
 Selsing, J., Fynbo, J. P. U., Heintz, K. E., & Watson, D. 2019, *GCN*, 23695, 1
 Tremou, L., Heywood, I., Vergani, S. D., et al. 2019, *GCN*, 23760, 1
 Ursi, A., Tavani, M., Frederiks, D. D., et al. 2020, *ApJ*, 904, 133
 Vereshchagin, G. V., & Aksenov, A. G. 2017, *Relativistic Kinetic Theory: with Applications in Astrophysics and Cosmology* (Cambridge: Cambridge Univ. Press)
 Vianello, G., Lauer, R. J., Younk, P., et al. 2015, arXiv:1507.08343
 Vuong, Q. H. 1989, *Econometrica*, 57, 307
 Wang, X.-Y., Liu, R.-Y., Zhang, H.-M., Xi, S.-Q., & Zhang, B. 2019a, *ApJ*, 884, 117
 Wang, Y., Li, L., Moradi, R., & Ruffini, R. 2019b, arXiv:1901.07505
 Watson, A. M., Butler, N., Becerra, R. L., et al. 2019a, *GCN*, 23749, 1
 Watson, A. M., Butler, N., Kutyrev, A., et al. 2019b, *GCN*, 23751, 1
 Wu, X. F., Dai, Z. G., Huang, Y. F., & Lu, T. 2003, *MNRAS*, 342, 1131
 Yost, S. A., Harrison, F. A., Sari, R., & Frail, D. A. 2003, *ApJ*, 597, 459
 Zeh, A., Klose, S., & Kann, D. A. 2006, *ApJ*, 637, 889
 Zhang, B. 2018, *The Physics of Gamma-Ray Bursts* (Cambridge: Cambridge Univ. Press)
 Zhang, B., Liang, E., Page, K. L., et al. 2007, *ApJ*, 655, 989
 Zhang, B., Wang, Y., & Li, L. 2021, *ApJL*, 909, L3
 Zhang, B.-B., Zhang, B., Castro-Tirado, A. J., et al. 2018, *NatAs*, 2, 69